DESCRIBING POST-GOE OXYGEN AVAILABILITY WITH TRACE METAL PALEOREDOX PROXIES

A Thesis
Presented to
The Academic Faculty

By

Josh David Stanford

In Partial Fulfillment
Of the Requirements for the Degree
Master of Science in Earth and Atmospheric Sciences

Georgia Institute of Technology

May 2017

Describing Post-GOE Oxygen Availability with Trace Metal Paleoredox Proxies

Approved by:

Dr. Chris Reinhard
School of Earth and Atmospheric Sciences
Georgia Institute of Technology

Dr. Jennifer Glass
School of Earth and Atmospheric Sciences
Georgia Institute of Technology

Dr. Ellery Ingall
School of Earth and Atmospheric Sciences
Georgia Institute of Technology

Dr. Yuanzhi Tang
School of Earth and Atmospheric Sciences
Georgia Institute of Technology

Date Approved: April 18, 2017

ACKNOWLEDGMENTS

J.D.S. acknowledges financial support from the National Aeronautics and Space Administration through the NASA Astrobiology Institute under Cooperative Agreement No. NNA15BB03A issued through the Science Mission Directorate and thanks K. Rybacki, X. Wang, D. Asael, and N. Planavsky for technical support.

TABLE OF CONTENTS

LIST OF TABLES

LIST OF FIGURES

LIST OF ABBREVIATIONS

Banded-Iron Formation	BIF
Billion years	Ga
Great Oxidation Event	GOE
Mass independent fractionation of sulfur	MIF-S
Million years	Ma
Present atmospheric level	PAL
Thousand years	kyrs

SUMMARY

Methods of describing local oxygen availability using coupled Mo isotopes and redox sensitive trace metal enrichments are applied to the Hotazel Iron Formation of the Transvaal Supergroup. These trace metal paleoredox proxies are used to track the presence of Mn-oxides in the ancient depositional environment, and an indication that Mn-oxides were present in the ancient environment implies local oxygenation. The Hotazel Formation was deposited in the wake of the GOE, and this sample set is utilized with the motivation of developing and calibrating a proxy for local oxygen availability. Indeed, the results suggest an oxygenated depositional environment, and therefore the findings of the work support the application of coupled Mo isotopes and trace metal enrichments to describe ancient oxygen availability. Moreover, since similar methods of oxygen detection have previously been applied to sediments deposited at 2.95 Ga, the results presented herein provide further support for locally oxygenated seawater and the advent of oxygenic photosynthesis by 2.95 Ga.

CHAPTER 1: INTRODUCTION

1.1 Scientific Motivation and Literature Review

The redox evolution of Earth's ocean–atmosphere system was the result of a host of dynamic processes unfolding over the past 4.5 billion years (Ga). The modern atmosphere contains 20.95% O_2, and the deep oceans are well oxygenated; however, throughout nearly half of Earth's history, the ocean-atmosphere system was largely devoid of oxygen. It is unknown what stimulated the rise in atmospheric oxygen, but an increase in the primary productivity of photosynthetic organisms, an increase in organic carbon burial, and a decrease in the buffering capacity of surface environments are likely the primary contributing factors [Catling et al., 2001; Holland, 2006; Kump and Barley, 2007; Kurzweil et al., 2016]. In any case, the disappearance of mass-independent fractionation of sulfur (MIF-S) signals from the sedimentary record indicates a rise in atmospheric oxygen above 10^{-5} present atmospheric level (PAL) ~2.45 Ga, and this transition in atmospheric redox state is termed the Great Oxidation Event (GOE) [Farquhar et al., 2000; Holland 2002]. The timing of ocean oxygenation is less precisely known, although geologic evidence suggests a significant lag between the rise in atmospheric oxygen and oxygenation of the deep oceans [Canfield, 1998; Arnold et al., 2004; Holland, 2006; Canfield et al., 2007; Canfield et al., 2008; Scott et al., 2008]. In fact, some studies suggest the deep oceans were not oxygenated until nearly two billion years after the initial rise in atmospheric O_2, but recent work indicates oxygen may have

begun to accumulate in shallow marine environments millions of years before the GOE [Kaufman et al., 2007; Kendall et al., 2010; Czaja et al., 2012; Olson et al., 2013; Planavsky et al., 2014a].

Understanding the evolution of the Earth system and the planet's pervasive biosphere necessitates a firm understanding of the prevailing oxygen availability through time, as oxygen deficiency may have delayed the evolution of complex life and driven mass extinctions. This relationship between complex life and molecular oxygen (O_2) is driven by the energetic capacity of oxygen as a terminal electron acceptor. Indeed, in using oxygen as a terminal oxidant, eukaryotic cells are able to achieve an ~8,000-fold increase in the energy flux supported by a given genome size [Lane and Martin, 2010]. Consequently, oxygen represents the only electron acceptor capable of meeting the metabolic demands for large and motile organisms such as metazoans [Catling et al., 2005]. As a function of this relationship between animal life and the oxygen cycle, oxygen deficiency is proposed as a major constraint of evolutionary and ecological expansion [Nursall, 1959; Planavsky et al., 2014b; Reinhard et al., 2016]. For example, widespread oxygen deficiency during the mid-Proterozoic (~1.8-0.8 Ga) may have been a primary contributing factor to the early rise yet prolonged diversification of eukaryotic organisms [Knoll, 2014; Reinhard et al., 2016]. Indeed, geochemical constraints in conjunction with quantitative models indicate substantial spatiotemporal variations in the oxygen content of the surface ocean and pervasive anoxia in the deep oceans during periods of Earth's history characterized by considerably lower atmospheric oxygen levels relative to today [Reinhard et al., 2016]. Further, these oxygen-lean conditions are offered as an explanation for the billion-year evolutionary hiatus leading up to the Cambrian

explosion -- colloquially referred to as the 'Boring Billion' [Planavsky et al., 2014b; Chen et al., 2015]. In fact, theoretical estimates for the minimum O_2 requirements of the last common ancestor of bilaterians are greater than the maximum estimates of atmospheric oxygen during the mid-Proterozoic. Furthermore, a significant temporal overlap is observed between the divergence of basal metazoan clades and the appearance of stable oxygenated environments capable of supporting animal life. Thus, it is difficult to deny an evolutionary coupling between animal life and the oxygen cycle.

In addition to driving evolution, oxygen availability may have also driven mass extinctions. In fact, paleoredox proxies indicate mass extinctions in the Late Devonian, Permian/Triassic, and Early Jurassic correspond to major ocean anoxic events [Wignall and Hallam, 1992; Bond et al., 2004; Knoll et al., 1996; Caruthers et al., 2013; Van de Schootbrugge et al., 2013; Planavsky et al., 2014b]. The most substantial extinction event corresponding to widespread benthic anoxia is the Late Permian mass extinction, which occurred approximately 250 million years ago (Ma). During this unparalleled extinction event, extinction at the genera and species levels reached 84-95%, and of most importance for the present study, fully half of the families of marine animals became extinct. While the Upper Permian rock record is characterized by over 500 families of marine animals, half of these are absent from the basal Triassic successions, and numerous studies suggest this rapid decline in marine life was the consequence of insufficient oxygen availability [Wignall et al., 1996; Knoll et al., 1996; Hotinski et al., 2001]. Hence, the aforementioned work demonstrates the intimate link between complex life and the oxygen cycle, and this relationship is a primary motivation for the present study.

Moreover, the motivation for this study is also derived from the function of O_2 as a biosignature gas. Since the only known mechanism for substantial oxygen accumulation is by way of oxygenic photosynthesis, the presence of molecular oxygen marks a substantial evolutionary milestone [Lyons et al., 2014]. A large body of work based on morphological features and molecular fossils suggest oxygenic photosynthesis predated the GOE, but the findings are inconclusive. For example, morphological features preserved in the Apex Chert have been interpreted to represent the presence of cyanobacteria ~3.47 Ga [Awramik, et al., 1983; Schopf and Packer, 1987; Schopf et al., 1993; Schopf et al., 2002, Schopf and Kudryavtsev, 2012]. These microfossils suggest oxygenic photosynthesis preceded the GOE by nearly one billion years; however, further studies determined that the ostensible microfossils may instead be formations produced through hydrothermal activity [Brasier et al., 2002; Brasier et al., 2015]. Subsequent research has attempted to track the presence of oxygenic photosynthesis through chemical signatures preserved in sedimentary rocks. As 2-methyl-bacteriohopanepolyols with an extended side-chain and more than 31 carbon atoms are ubiquitously produced by cyanobacteria, their hydrocarbon derivatives, 2α-methylhopanes, are interpreted as the molecular fossils of these organisms [Summons et al., 1999]. While 2-methylhopanes are present in 2.7 Ga sedimentary rocks, additional work shows that the biomarkers migrated into the rocks no later than 2.2 Ga [Rasmussen et al., 2008]. Furthermore, 2-methylhopanes are also produced by anoxygenic phototrophs, so these biomarkers do not conclusively represent evidence for oxygenic photosynthesis [Rashby et al., 2007]. Although biomarkers and morphological features yield ambiguous estimates for the advent of oxygenic photosynthesis, tracking the presence of oxygen using trace metal

geochemistry has emerged as a promising tool in constraining this major evolutionary event.

Herein, trace metal enrichments and Mo isotopes are used in concert to describe the redox chemistry, and specifically the oxygen availability, during deposition of the Hotazel Formation of the Transvaal Supergroup. The results are best viewed as an attempt to develop and calibrate a technique coupling redox sensitive metal enrichment and Mo isotope systematics as a proxy for local oxygen availability. Moreover, the results can be applied to previous work describing oxygen availability by way of similar rationale.

1.2 Molybdenum Geochemistry and Isotope Systematics

The unique geochemical attributes of Mo place it at the forefront of the tools used to trace oxygen availability in ancient environments. The primary source of Mo to modern oceans is through oxidative weathering of the continental crust and subsequent riverine delivery of molybdate (MoO_4^{2-}) [Bertine and Turekian, 1972; Siebert et al., 2003]. Low-temperature hydrothermal systems also input Mo to the oceans, but this input is only approximately 10% of the riverine source [Siebert et al., 2003]. Molybdate is a tetrahedrally coordinated oxyanion with low reactivity under oxic conditions [Erickson and Helz, 2000]. The inertness of molybdate in oxic settings is the result of strong covalent bonding preventing substitutive and reductive reactions, and molybdate's conservative behavior results in a long residence time in modern oceans of approximately 800 kyrs [Morford and Emerson, 1999]. In fact, Mo is the most abundant transition metal

in the modern ocean, with a concentration of approximately105 nM [Emerson and Huested, 1991]. While oxic and suboxic sinks are important removal pathways in the modern oceans, the Mo burial flux is greatest under anoxic settings. Indeed, Mo is readily removed from solution under anoxic settings through adsorption to humic substances, uptake in solid solution with Fe-sulfides, and adsorption to Fe-Mn-oxyhydroxides (henceforth referred to as Fe- and Mn-oxides) [Morse and Luther 1999; Adelson et al., 2001; Barling et al., 2001; Algeo and Lyons, 2006]. Further, Mo removal under anoxic settings is facilitated by the formation of particle reactive thiomolybdates ($MoO_{4-x}S_x^{-2}$), since thiomolybdates are readily scavenged from solution [Helz et al., 1996; Erickson and Helz, 2000]. Therefore, given a sufficient supply of Mo, sediments depositing under anoxic and sulfidic (euxinic) settings will commonly be characterized by elevated authigenic Mo enrichment, and consequently, Mo is often highly concentrated in black shales [Calvert and Pedersen, 1993].

Since Mo is supplied to rivers and eventually oceans through the oxidative weathering of continental crust, the concentration of dissolved Mo in the oceans is in part a product of the degree of oxidative weathering; however, as molybdate is stable and largely unreactive under oxic settings and readily transferred to sediment under anoxic settings, the Mo concentration of the oceans is primarily controlled by the extent of ocean oxygenation [Anbar et al., 2007; Scott et al., 2008]. Expanding anoxia will decrease the oceanic Mo reservoir, as molybdate interacting with H_2S will be converted to particle-reactive thiomolybdates and subsequently scavenged from solution. Therefore, the Mo enrichments of euxinic black shales will diminish as deep ocean anoxia expands because a given input of Mo will be removed from solution over a greater area. It follows that

expanding oxic deep waters will allow the dissolved Mo concentration to increase, and a corresponding increase in euxinic black shale Mo enrichments will ensue. Hence, Mo enrichments in euxinic black shales are reflections of the size of the oceanic Mo reservoir as well as the extent of deep ocean oxygenation [Scott et al., 2008].

The continental crust contains ~1-2 ppm Mo on average, while euxinic black shales of the Archean, Proterozoic, and Phanerozoic contain an average Mo concentration of 3, 18, and >100 ppm, respectively [Anbar et al., 2007]. Mo enrichments in euxinic black shales covering the last 2.7 Ga are suggested to represent the progressive oxygenation of the deep oceans, thus the increased enrichments characterizing the Phanerozoic are interpreted as evidence for the onset of widespread deep ocean oxygenation [Scott et al., 2008]. Additionally, a spike in the concentration of Mo in the Archean Mount McRae black shale is interpreted as a transient, mild episode of oxygenation, referred to as a "whiff" of oxygen before the Great Oxidation Event [Anbar et al., 2007]. Although Mo enrichment is a powerful proxy for studying ancient redox conditions, it is not the most robust method for detecting localized and/or transient oxygen availability.

The burial flux of Mo is greatest under anoxic settings, but Mo is also removed from solution under oxic settings. Indeed, in oxygenated environments, the primary Mo sink is by adsorption of molybdate onto Mn- and Fe-oxides, and this removal pathway can be traced through Mo isotope signatures [Erickson and Helz, 2000; Barling and Anbar, 2004; McManus et al., 2006; Goldberg et al., 2009]. The average δ^{98}Mo of riverine input to the oceans is estimated to be approximately 0.7 per mil [Archer and Vance, 2008]. This input estimate is the discharge- and total-Mo-weighted signature of a

host of globally distributed modern rivers. The $\delta^{98}Mo$ value of modern mean open ocean water (MOMO) is ~2.3 per mil, and the offset between $\delta^{98}Mo_{MOMO}$ and $\delta^{98}Mo_{riverine\ input}$ must therefore be related to Mo removal from seawater [Siebert et al., 2003; Barling and Anbar, 2004; Arnold et al., 2004]. As stated previously, the primary Mo sink under oxic settings is by adsorption of molybdate onto Mn- and Fe-oxides. Adsorption onto Mn-oxides induces a transformation from tetrahedral to octahedral coordination and a corresponding equilibrium fractionation, where adsorbed Mo is approximately 2.7 per mil lighter than Mo in solution [Siebert et al., 2003; Kashiwabara et al., 2011]. Further, $\Delta^{98}Mo_{soln\text{-}MnOx}$ is relatively insensitive to variations in pH, temperature, and ionic strength over ranges relevant for seawater [Barling and Anbar, 2004; Wasylenki et al., 2008]. Most importantly, the presence of Mn-oxides indicates the presence of free oxygen. In fact, the rate of Mn oxidation is controlled by O_2 concentrations, and the oxidation rates are consistent with Michaelis-Menten type kinetics [Clement et al., 2009; Planavsky et al., 2014a].

Similar to the adsorption of Mo by Mn-oxides, Mo that adsorbs onto Fe-oxides is also isotopically lighter than Mo in solution; however, the fractionation is not as large as that associated with adsorption onto Mn-oxides. In fact, depending on the mineralogy of the depositing Fe-mineral, the fractionation may fall between 0.83 and 2.19 [Goldberg et al., 2009]. The following Fe-minerals are listed in order of increasing $\Delta^{98}Mo_{soln\text{-}FeOx}$: magnetite (~0.83 per mil), ferrihydrite (~1.1 per mil), goethite (~1.4 per mil), and hematite (~2.19 per mil). The equilibrium fractionation associated with adsorption onto Fe-oxides is a function of the proportion of adsorbed octahedral versus tetrahedral Mo species, where a greater proportion of adsorbed octahedral species is characterized by a

greater magnitude of isotopic fractionation [Kashiwabara et al., 2011]. Additionally, $\Delta^{98}Mo_{soln\text{-}FeOx}$ is affected by pH, with slightly greater fractionation occurring at higher pH, but the effects of pH on fractionation are only ~0.1 per mil at pH values relevant to seawater. As a result of the different fractionations arising through Mo adsorption onto Fe- relative to Mn-oxides, sediments depositing under oxygenated seawater should be characterized by a positive correlation between $\delta^{98}Mo$ and Fe/Mn concentrations [Planavsky et al., 2014a]. A positive correlation between $\delta^{98}Mo$ and Fe/Mn concentrations is observed in 2.95 Ga sediments, but this correlation has not been reported in younger sediments [Planavsky et al., 2014a]. The primary objective of this study is to test the ability of the aforementioned relationship between $\delta^{98}Mo$ and Fe/Mn concentrations to track the presence of free O_2, by applying this proxy to iron and manganese ore deposited approximately coeval but likely several million years following the GOE. The ultimate aim is to further develop this tool for robustly detecting and describing ancient oxygen oases.

CHAPTER 2: Materials and Methods

2.1 Geologic Setting

The Transvaal Supergroup located in the Kaapvaal Craton of South Africa and Botswana hosts volcanic and sedimentary rocks of the late Archean and Paleoproterozoic (2.7-2.05 Ga); (Figure 1A) [Tsikos and Moore, 1997; Moore et al., 2001]. The preserved sequences are exposed in two geographically distinct regions termed the Transvaal Basin and the Griqualand West Basin, which are separated by the Vryburg arch. The present study focuses on the Hotazel Formation of the Griqualand West Basin in the Northern Cape Province of South Africa (Figure 1B). The lower portion of the Transvaal Supergroup in this region is comprised of the Ghaap Group, which includes primarily platform carbonates and iron formations formed between 2,588 +/- 6 and 2,521 +/- 3 Ma (Figure 2B) [Gumsley et al. 2017]. Previous work has suggested that the upper portion of the Supergroup, the Postmasburg Group, unconformably overlies the Ghaap Group, but recent work indicates no major discontinuity between the Groups [Kirschvink et al., 2000; Moore et al., 2001]. The Makganyene Formation (150 m) is a glacial diamictite composed of poorly sorted clasts and occasional dropstones that forms the base of the Postmasburg Group [Tsikos and Moore, 1997]. The U-Pb age derived for the Makganyene formation is 2,436 +/- 14 Ma [Gumsley et al., 2017]. Furthermore, the Makganyene glacial deposits are approximately coeval with the overlying subaqueous pillow lavas of the Ongeluk Formation [Evans et al., 1997]. Indeed, the two formations

interfinger, and the uppermost layers of the Makganyene contain small volcanic fragments. The Ongeluk Formation (up to 900 m thick) is composed of basaltic andesite flows, and paleomagnetic data indicate the lava flows, in addition to the glacial sediments, were deposited at low latitudes (11°+/- 6°) [Evans et al., 1997; Tsikos and Moore, 1997; Gumsley et al., 2017]. Further, the U-Pb age derived for the Ongeluk lava flows is 2,424 +/- 32 Ma, and thus the interfingering low latitude glacial deposits are evidence for a snowball earth episode beginning ~2.44 Ga and ending ~2.42 Ga [Cornell et al., 1996; Kirschvink et al., 2000; Kopp et al., 2005; Gumsley et al., 2017].

The Hotazel Formation conformably overlies the Ongeluk Formation, and this formation is characterized as the youngest iron formation of the Transvaal Supergroup [Tsikos and Moore, 1997]. Moreover, the Hotazel Formation is composed of four separate units of Superior-type banded-iron formations (BIF) interbedded with three manganese layers and covers an area of approximately 400 km^2 known as the Kalahari manganese field (Figure 1B and 2A) [Tsikos et al., 2010]. In fact, the approximately eight billion tons of Mn ore hosted within the ~100 m thick Hotazel Formation represent approximately 50% of the total known land-based manganese resources, and thus the Hotazel represents the largest known land-based manganese reservoir [Tsikos et al., 2003]. The basal unit of the Hotazel is a ~1 m jaspilitic iron stone with small occasional dropstones, which suggest the onset of this formation coincided with deglaciation [Kirschvink et al., 2000]. The remaining BIF portions of the Hotazel are generally composed of mm to cm scale laminated assemblages dominated by approximately equal proportions of micro-crystalline quartz and magnetite [Tsikos et al., 2010]. Diagenetic carbonates represent the second most abundant species (ankerite and calcite), and Fe-

silicates (greenalite, minnesoataite, and stilpnomelane) represent the third. The BIF mineralogy indicates the Hotazel sediments are characterized by a very shallow burial metamorphic overprint of less than 200° C [Gutzmer and Beukes, 1996; Tsikos et al., 2003; Tsikos et al., 2010]. The manganese rich layers of the Hotazel are primarily composed of variable proportions of very fine-grain braunite and hematite, but these layers can also contain a substantial fraction (up to 40%) of manganiferous carbonate [Tsikos et al., 2010]. Furthermore, the contacts between BIF and manganese layers are primarily composed of fine-grain hematite and diagenetic Mn-carbonates such as kutnahorite, Mn-calcite, and Mn-dolomite, and these transitional units vary in thickness from several decimeters to several meters. The BIF and manganese layers vary in thickness across the formation as well, where the lower, middle, and upper manganese layers reach 45, 3, and 10 meters, respectively [Tsikos and Moore, 1997]. In contrast, the thicknesses of the BIF layers are generally antiphased with the manganese layers and vary between ~5 and ~45 m in thickness. It is important to note that while discrete sections of the Hotazel contain an abundance of carbonate minerals, the carbonate-rich units are not analyzed in this study. Furthermore, the drill-core used for this study is composed of rocks lacking visible secondary effects of supergene oxidation or hydrothermal alteration [Tsikos et al., 2010]. In addition, the Mn mineralogy suggests a burial metamorphic overprint of less than 200 °C. Finally, Mn concentrations in veins of the Hotazel Formation were tested to determine whether metasomatic fluids could have delivered the Mn to the Hotazel Formation, but the Mn enrichments are restricted to the three interbedded regions of the stratigraphic column [Johnson et al., 2013].

The Mooidraai Formation (~300 m thick) comformably overlies the Hotazel Formation and is primarily composed of dolomite and chert [Tsikos et al., 1997, Bau et al., 1999]. The whole-rock Pb-Pb derived age of the Mooidraai Formation is ~2,394 +/- 26 Ma [Tsikos et al., 2003; Gumsley et al., 2017]. The Hotazel Formation is thus bracketed between ~2.42 and ~2.39 Ga. Importantly, recent U-Pb dating indicates the GOE occurred between 2,460 and 2,436 +/- 3 Ma, which is roughly coincident and likely at least several million years prior to the deposition of the Hotazel Formation [Gumsley et al., 2017]. In addition, the negative Ce anomaly of the Hotazel Formation indicates deposition after the onset of the GOE [Bau, 2006]. Therefore, multiple lines of evidence suggest the Mn and Fe ore of the Hotazel Formation were deposited during and/or after the atmosphere transitioned from anoxic to oxic conditions.

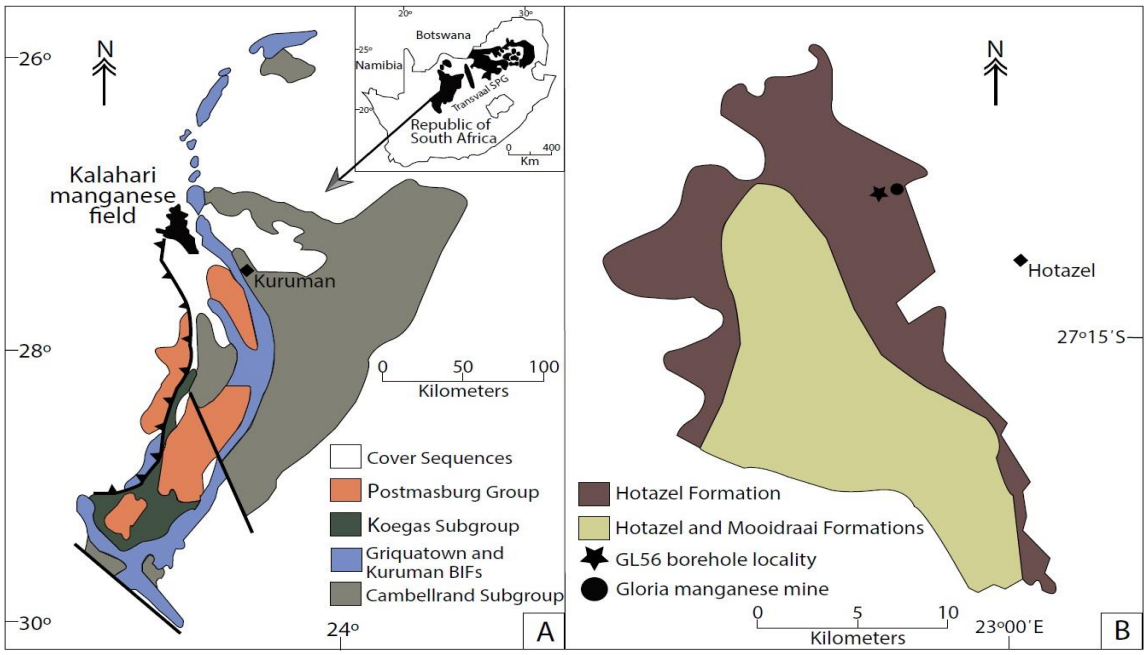

Figure 1. (A) Geographic location of the Transvaal Supergroup in South Africa (inset), and the regional geologic map of the Transvaal Supergroup in Northern Cape Province illustrating the location of the Kalahari manganese field, structural features, and the major lithostratigraphic subdivisions. (B) Map of the Kalahari manganese field including major structural features in addition to relevant mine and drillcore localities. Figure 1A and 1B are modified after Tsikos et al., 2010.

2.2 Sample Preparation and Chemical Characterization

For this study, 22 quarter-core samples from drill core GL56 of the Gloria Mine were utilized (Figure 1B). Quarter-core samples were chipped in ceramic chipmunk jaw crusher. The rock chips were then powdered in an alumina ceramic dish within a SPEX Shatterbox. Chemical procedures were performed under metal-free conditions in polypropylene laminar flow hoods using distilled acids (HNO_3; HCl) and/or trace metal grade HF. Rock powder digestion was performed by dissolving ~750 mg of powder with 5 mL concentrated HNO_3 and 1 mL concentrated HF in PFA vials. Samples were then

sonicated for 1 hour before being heated overnight on a hotplate at 150 °C. Next, the vials were uncapped and evaporated at 150 °C. Once the liquid had evaporated and a damp residue remained, samples were redissolved in 4 mL aqua regia (3:1 concentrated HCl:HNO_3). After adding aqua regia, samples were sonicated for 1 hour before being heated overnight on a hotplate at 150 °C. As before, samples were then uncapped and evaporated until all liquid evaporated and remaining residues were damp. Next, 1 mL concentrated HCl was added to each sample, and vials were added back to the hotplate and evaporated. After this final evaporation, samples were redissolved in 50% HCl for storage, and a fraction was removed and diluted in 50% HNO_3 for ICP-MS analysis. Elemental concentrations were measured using a Thermo-Finnegan Element XR ICP-MS at Yale University.

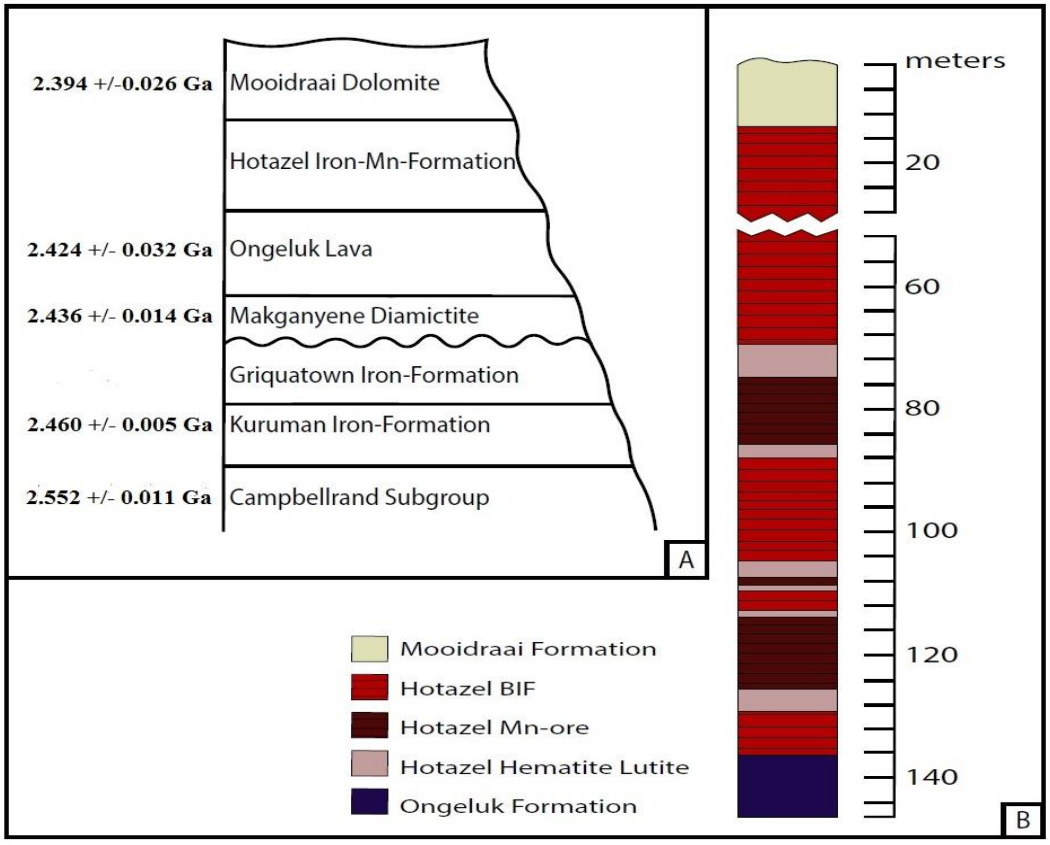

Figure 2. (A) An illustration of the simplified stratigraphy of the Transvaal Supergroup and approximate ages of the formations. Modified after Bau et al., 1999 to include more recent dating data from Gumsley et al., 2017. (B) Stratigraphic column of the Hotazel Formation in the northern Kalahari manganese field. The column illustrates the general mineralogical characteristics and relative thickness relations between BIF, Mn-ore, and hematite-lutite transitional layers. Actual thicknesses of these layers can vary depending on geographic location. Modified after Tsikos et al., 2010.

2.3 Mo Isotope Measurements

Using the measured Mo concentrations, a double spike was added to each sample at a 1:1 sample:spike ratio, so that the total [Mo] of each sample was 200 ppb. The double spike contained equal proportions of ^{95}Mo and ^{97}Mo and was prepared

gravimetrically from Oak Ridge Laboratory metal powders. Molybdenum purification was completed through a two-stage column technique outlined in Table 1. The first stage anion exchange separates Mo and most Fe from the matrix, while the second stage cation exchange separates Mo from remaining Fe. As a result of the extremely high Fe content of the samples, it was not possible to quantitatively retain the Mo of each sample in the resin. As a result, the Mo yields for each sample were approximately 20%. The Mo isotope measurements were completed using a Thermo Neptune MC-ICP-MS at Yale University. All Mo isotope data are reported relative to standard NIST-3134 using the following conventional delta notation:

$$\delta^{98}\text{Mo}\ (‰) = [(\delta^{98}\text{Mo}/\ \delta^{95}\text{Mo})_{\text{sample}}/(\delta^{98}\text{Mo}/\ \delta^{95}\text{Mo})_{\text{NIST-3134}}\text{-}1]*1000.$$

During Mo isotope analyses, frequent measurements of USGS Manganese Nodule Standard NOD P-1 were also taken, and these results are displayed in Table 2. The long-term external reproducibility is 0.1 ‰.

Table 1. Chromatography procedure for Mo and Fe columns

Step	Reagent	Volume (mL)
Stage I anion exchange		
Wash	H_2O	8
Wash	0.5 N HNO_3	4
Wash	H_2O	4
Wash	2 N HCl	4
Wash	H_2O	4
Conditioning	7 N HCl	4
Sample loading	7 N HCl	1
Matrix rinse	7 N HCl	2*2.25
Cu	7 N HCl	3*6
Fe	2 N HCl	2*2
Mo	0.5 N HNO_3	3*5
Wash	H_2O	8
Wash	0.5 N HNO_3	4
Wash	H_2O	4
Stage II cation exchange		
Wash	H_2O	8
Wash	6 N HCl	4
Wash	0.24 N HCl	4
Conditioning	0.24 N HCl	4
Sample	0.24 N HCl	1
Mo	0.24 N HCl	3*3
Fe	6 N HCl	2*3
Wash	H_2O	8
Wash	6 N HCl	4
Wash	H_2O	4

Table 2. δ^{98}Mo values measured for the Nod P-1 standard relative to Mo NIST-3134.

Standard	δ^{98}Mo (‰)	2SD
Nod P-1 (1)	-0.89	0.03
Nod P-1 (2)	-0.95	0.02

CHAPTER 3: Results

3.1 Elemental Concentrations

The concentrations of Mo, Mn, Fe, Co, Ni, and Sr measured in the Hotazel samples are displayed in Table 3. Strong covariation is observed amongst the concentrations of select metals, but stratigraphic trends are absent from the data. The concentrations of Mo and Mn in the sediments range from 0.05 to 3.38 ppm and 0.03 to 49.31 wt%, respectively, and a strong positive correlation is observed between their concentrations (R^2=0.99; Figure 3A). Furthermore, the concentration of Fe ranges between 0 and 43.53 wt%, and Fe concentrations negatively correlate with both Mn and Mo concentrations. Further, a negative correlation between Fe/Mn and Mo content is observed (R^2=0.89; Figure 3B). Similar to Mo, Co concentrations vary positively and negatively with Mn and Fe content, respectively (R^2=0.89 and R^2=0.88, respectively; Figure 3C and 3D, respectively). The Co concentrations in the formation vary between 0.38 ppm and 66.20 ppm, and a positive correlation between Co and Mo concentrations is observed (R^2=0.78; Figure 4A). In addition, Ni concentrations range between 0.94 and 17.10 ppm, and correlations between Ni concentrations and Fe/Mn concentrations are comparable to those observed between both Co and Mo with Fe/Mn; although, the correlations with Ni are not as strong (R^2=0.73; Figure 4B). Further, Sr concentrations range between 3.16 and 360.81 ppm, and a similar correlation is also observed between Fe/Mn and Sr concentrations as Fe/Mn and Mo, Ni, and Co, respectively (R^2=0.78;

Figure 4C). Very weak correlations (R^2<0.2) are observed between Fe/Mn and V, Cr, and U concentrations. Although Fe/Mn correlates more strongly with U than V, Cr, and U, the relationship is still weak (R^2=0.45).

3.2 Mo Isotope Compositions

The δ^{98}Mo values range between 1.31 and -1.15‰, and the average value is 0.19 ‰ (n=24; Table 3). Of the 24 samples, thirteen are characterized by positive δ^{98}Mo values, ten are negative, and one is approximately zero. There are no stratigraphic trends in δ^{98}Mo values, but there are correlations between δ^{98}Mo values and metal concentrations. A moderate correlation is observed between δ^{98}Mo and Fe/Mn (R^2=0.56; Figure 5A). The most Fe-rich samples are generally characterized by the most positive δ^{98}Mo values. Conversely, the most negative δ^{98}Mo values are measured in the most Mn-rich samples, although some Mn-rich samples are characterized by moderately positive δ^{98}Mo values extending up to 0.41 ‰. Additionally, moderate correlations are also observed between δ^{98}Mo and both Co and Ni concentrations (R^2=0.60 and 0.61, respectively; Figures 5B and 5C, respectively). Very weak correlations (R^2 <0.30) are observed between δ^{98}Mo and V, Cr, and U. Furthermore, the relationship between Fe/Mn and δ^{98}Mo observed in the Hotazel agrees with the relationship observed in Planavsky et al., 2014a, and both datasets are plotted together in Figure 5D (R^2=0.50).

Table 3. Data summary for Hotazel samples from drill core GL56 and Nod P-1 standards

Depth (m)	$\delta^{98/95}$Mo (‰)	2σ	Mo ppm	Mn wt%	Fe wt%	Fe/Mn	Co ppm	Ni ppm	Sr ppm
193.05	1.31	0.83	0.05	0.03	43.53	1548.98	0.58	0.94	3.14
259.50	0.59	0.66	0.24	0.59	37.42	63.64	1.04	1.22	17.37
260.90	1.40	0.12	0.39	0.76	25.44	33.69	1.82	1.54	82.94
271.45	0.88	0.06	0.30	0.84	17.94	21.25	0.93	1.60	37.73
273.13	0.33	0.31	0.28	0.67	0.00	0.00	0.63	1.54	9.40
274.37	0.84	0.04	0.41	1.12	21.24	19.05	1.36	2.00	16.52
275.42	0.23	0.05	1.24	16.82	6.36	0.38	32.05	7.13	141.81
275.90	-0.07	0.05	1.30	17.09	6.67	0.39	36.84	7.84	266.20
276.30	-0.97	0.10	1.22	17.71	6.77	0.38	60.44	7.24	236.53
276.93	-0.42	0.59	2.25	29.89	16.36	0.55	52.66	8.74	247.39
277.75	-0.75	0.06	2.89	40.95	6.41	0.16	62.97	9.85	360.81
275.90	-0.13	0.04	1.18	17.04	6.60	0.39	36.63	7.86	228.31
279.33	0.12	0.12	3.00	41.16	9.82	0.24	53.06	9.78	285.89
280.91	0.00	0.06	2.55	40.10	4.82	0.12	52.93	10.84	218.56
282.35	-0.04	0.10	2.01	29.71	3.51	0.12	38.45	11.30	286.51
285.59	-1.15	0.07	2.55	48.71	5.45	0.11	44.73	10.11	183.07
288.28	0.41	0.08	2.01	49.31	4.64	0.09	48.18	9.93	161.41
290.69	-0.07	0.05	3.37	44.38	4.50	0.10	30.41	6.83	92.64
291.50	-0.28	0.21	3.38	25.33	7.72	0.30	66.20	11.81	89.40
293.08	0.39	0.26	3.15	24.42	16.42	0.67	30.23	4.91	39.70
295.08	0.42	0.40	1.78	4.19	34.79	8.30	17.37	3.11	9.88
297.05	0.56	0.26	1.91	2.98	28.16	9.45	6.16	1.03	9.28
301.28	1.22	0.07	0.54	0.05	25.38	552.45	0.38	1.27	3.63
374.85	-0.30	0.03	0.63	1.28	15.26	11.95	10.12	17.11	9.83
Nod P-1 (1)	N/A	N/A	655.32	39.94	58.74	0.15	2404.15	13817.51	649.92
Nod P-1 (2)	N/A	N/A	656.06	38.84	58.45	0.15	2347.13	13647.82	652.65
Nod P-1 (3)	N/A	N/A	649.96	39.22	55.69	0.14	2262.54	13157.46	641.88

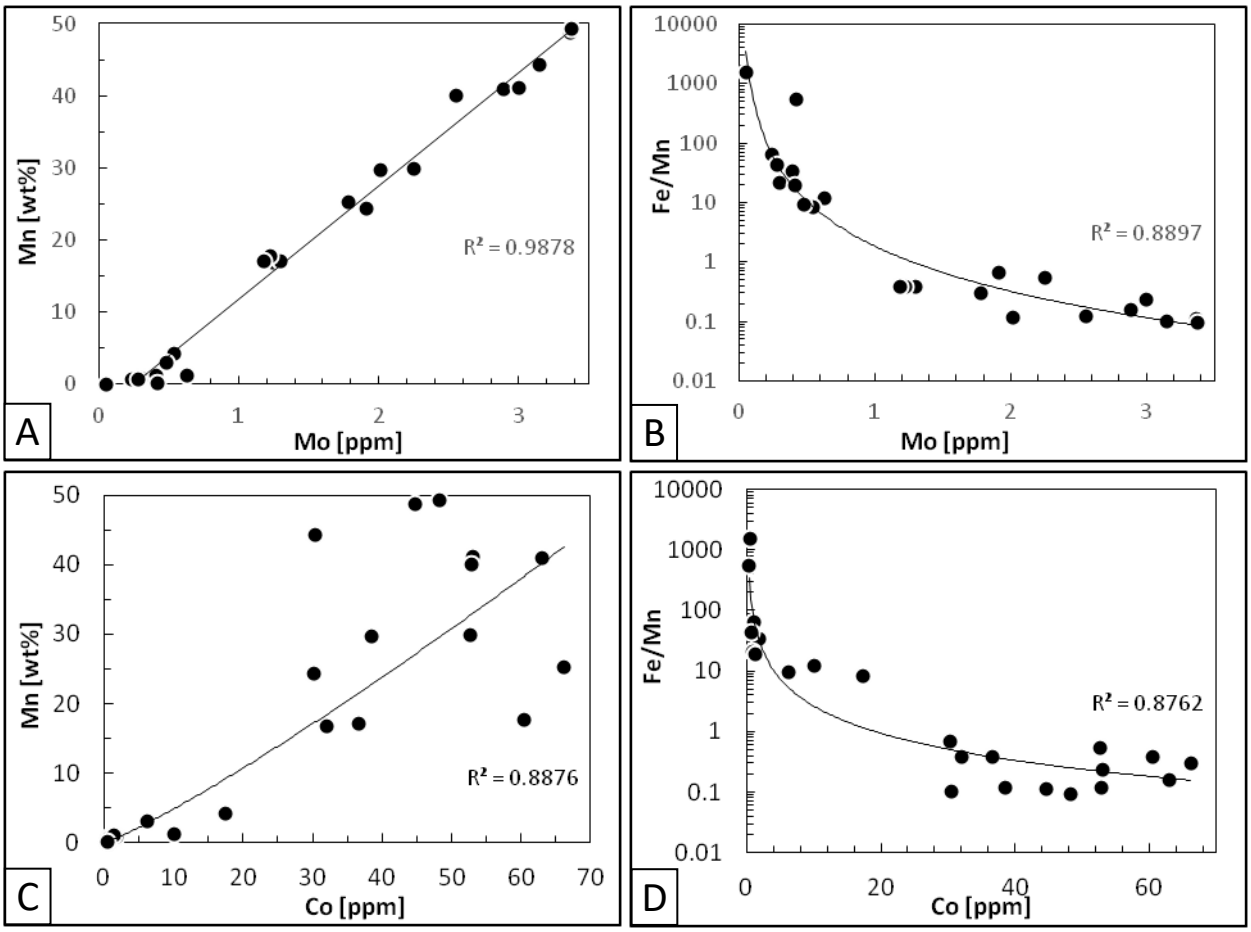

Figure 3. Relationships between trace metal enrichments (A) Mn [wt%] is plotted against Mo [ppm] with a linear fit and an R^2=0.99. This relationship indicates a strong coupling between their delivery mechanisms to sediment. (B) Fe/Mn values are plotted against Mo [ppm] with a power fit and an R^2=0.89. This relationship indicates the deposition of Mo is more closely related to Mn deposition than Fe deposition. (C) Mn [wt%] is plotted against Co [ppm] with a power fit and an R^2=0.89. This relationship indicates a coupling of their delivery mechanisms to sediment. (D) Fe/Mn values are plotted against Co [ppm] with a power fit and an R^2=0.88. This relationship suggests the deposition of Co is more strongly influenced by Mn than Fe deposition.

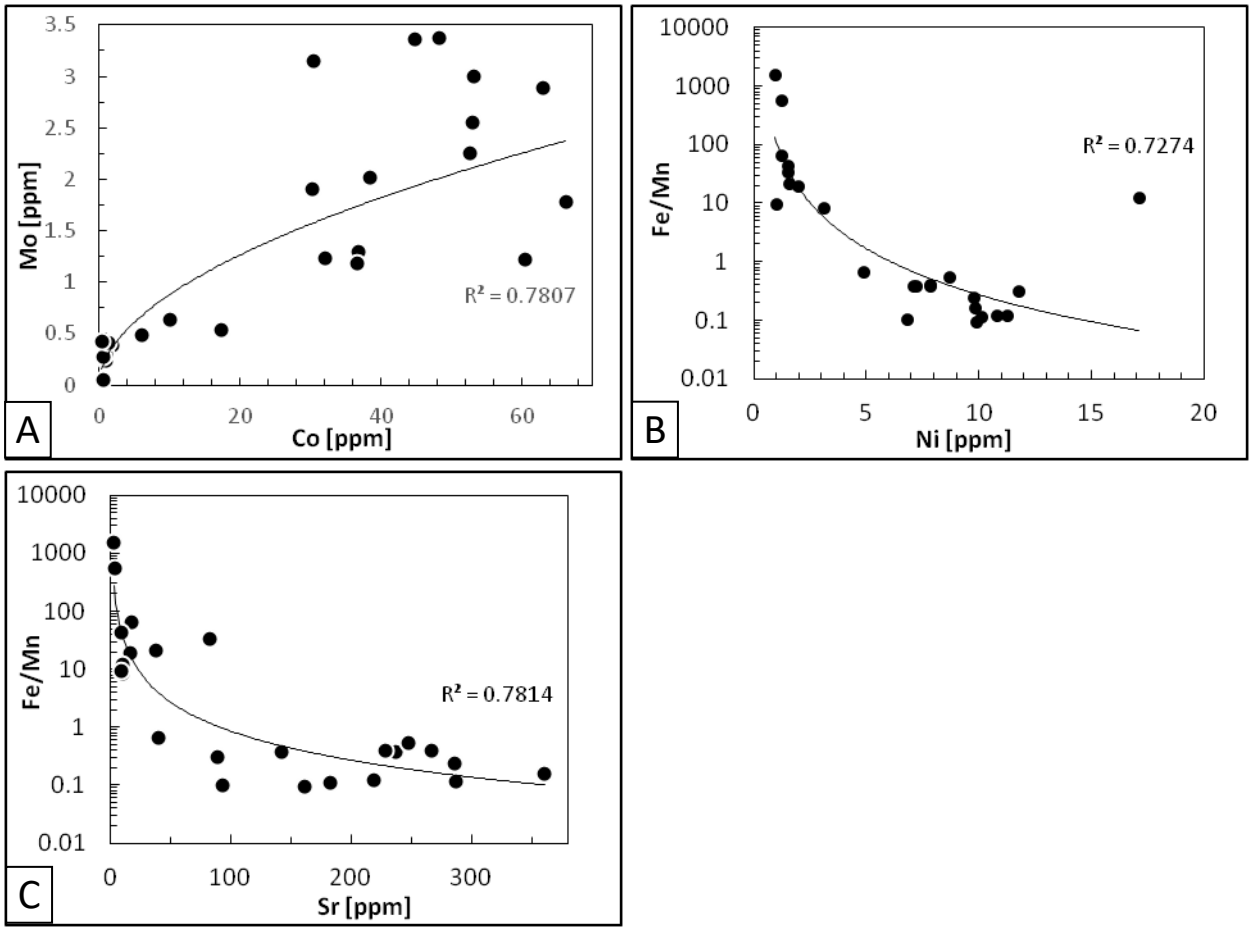

Figure 4. Additional relationships between trace metal enrichments (A) Mo [ppm] is plotted against Co [ppm] with a power fit and an R^2=0.78. The relationship suggests a coupling between the Mo and Co depositions. (B) Fe/Mn values are plotted against Ni [ppm] with a power fit and an R^2=0.73. The relationship suggests that the deposition of Ni is more strongly coupled to Mn than Fe deposition. (C) Fe/Mn values are plotted against Sr [ppm] with a power fit and an R^2=0.78. The relationship indicates that Sr deposition is also more strongly coupled to the deposition of Mn than the deposition of Fe.

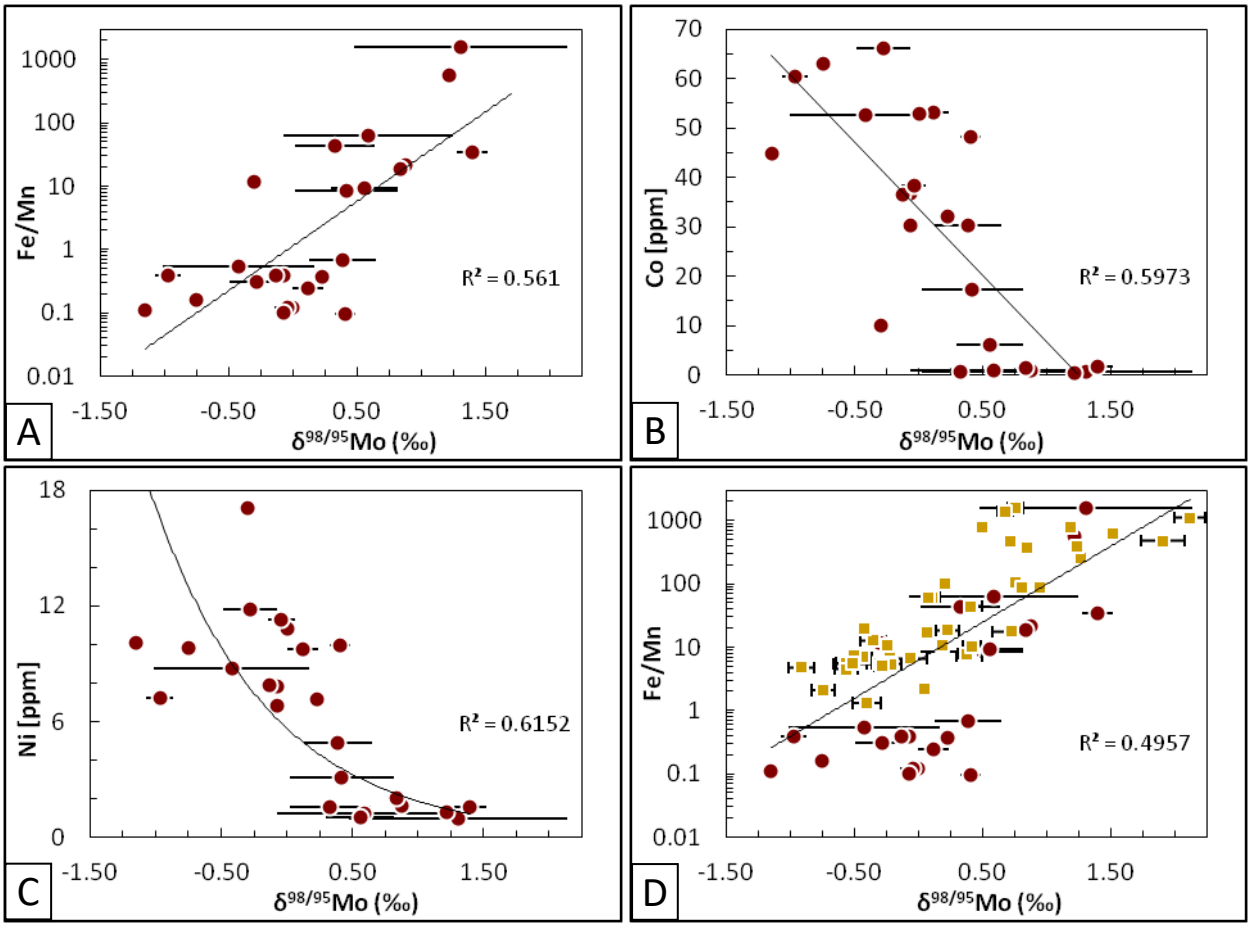

Figure 5. Relationships between Mo isotope values and trace metal enrichments (A) Fe/Mn values are plotted against δ^{98}Mo values with an exponential fit and $R^2 = 0.56$. This relationship suggests Mn-oxides were delivering relatively light Mo isotopes to sediment, while Fe-oxides were delivering heavier Mo to sediment. (B) Co concentrations [ppm] are plotted against δ^{98}Mo values with a linear fit giving $R^2 = 0.60$. The correlation suggests the same mechanism enriching sediments in Co may also be enriching sediments in light Mo isotopes. (C) Ni concentrations [ppm] and δ^{98}Mo values are plotted with an exponential fit giving $R^2 = 0.62$. The relationship suggests that the mechanism delivering light Mo isotopes to sediment may also be enriching sediments in Ni. (D) Fe/Mn is again plotted against δ^{98}Mo values with an exponential fit yielding $R^2 = 0.50$, where the red circles represent the Hotazel data from this study, and the yellow squares represent iron stone data from the Sinqeni Formation (~2.95 Ga), the Parktown Formation (~2.95), the Manjeri Iron Formation (~2.70 Ga), the Timeball Hill Formation (~2.32 Ga), and the Animikie Basin Iron Formation (~1.88 Ga) [Planavsky et al., 2014a]. The agreement between datasets suggests the same mechanism delivering Mo to sediments during/following the GOE was also delivering Mo to sediments 500 Ma before the GOE.

CHAPTER 4: Discussion

4.1 Trace Metal Enrichments

The concentration of Mo in the Hotazel Formation is very low relative to modern Fe-Mn deposits, but the values are approximately average for Archean and Paleoproterozoic Fe-Mn deposits. Indeed, ferromanganese oxide sediments, crusts, and nodules on the modern seafloor often contain 100's to 1,000's ppm Mo [Bertine and Turkein, 1973; Anbar, 2004]. Conversely, iron stones of the Archean and Paleoproterozic often contain 100's to 1,000's ppb Mo [Planavsky et al., 2014a]. Similarly, Phanerozoic black shales are characterized by 100's ppm Mo, whereas Precambrian black shales generally contain less than 50 ppm Mo [Scott et al., 2008]. Therefore, whether the depositional environment was poorly oxygenated or well oxygenated, Mo becomes increasingly enriched in younger sediments. Anoxic sediments may become enriched in Mo through adsorption to humic substances, uptake in solid solution with Fe-sulfides, or adsorption to Fe-Mn-oxides, while oxic sediments become enriched in Mo primarily through adsorption to Fe-Mn-oxides [Calvert and Pedersen, 1993; Algeo and Lyons, 2006]. The inverse relationship between Mo enrichment and age is likely a reflection of the size of the oceanic Mo reservoir, where increased rates of oxidative weathering and increased ocean oxygenation support a larger Mo reservoir [Scott et al., 2008]. It is therefore not surprising that the sediments of the Hotazel Formation are characterized by low Mo concentrations relative to modern Fe-Mn deposits, since the deposition of the

Hotazel Formation occurred nearly two billion years before the ocean became well oxygenated [Scott et al., 2008]. Hence, the low Mo concentrations of the Hotazel Formation may reflect an ocean that was largely devoid of oxygen and consequently characterized by a vanishingly small Mo reservoir.

In oxygenated seawater, Mo absorbs onto Mn-oxides, and as a result, sediments rich in Mn-oxides are often also rich in Mo [Calvert and Pedersen 1993; Siebert et al., 2006]. Within the Hotazel Formation, Mn is primarily hosted in braunite and Mn-carbonate phases [Tsikos et al., 2010]. Braunite is a mixed valence Mn-silicate containing Mn(II) and Mn(III), and as the oxidation of Mn(II) to Mn(III) or Mn(IV) requires a high potential oxidant, the presence of oxidized Mn-phases suggests the presence of molecular oxygen in the depositional environment [Johnson et al., 2013]. Therefore, the oxidized Mn phases in the Hotazel are the first indication that the seawater in this region may have been oxygenated [Kirschvink et al., 2000; Roy, 2000]. Since a primary vector of Mo transport to sediments is through the adsorption onto Mn-oxides, the strong positive correlation between Mo and Mn provides further indication for Mn-oxides, and thus O_2 in the water column (Figure 3A). Importantly, as sinking Mn-oxides reach the sediment-water interface, dissolution and liberation of adsorbed Mo may occur. Upon reduction, Mn-oxides will dissolve and release the adsorbed Mo to pore waters and potentially the overlying water column; however, the final sedimentary hosts of both Mn and Mo are carbonate phases [Scott and Lyons, 2012; Johnson et al., 2013; Kurzweil et al., 2016]. In fact, the process by which Mn-oxides are transported out of the water column and deposited within marine sediments as carbonates is referred to as the ‘manganese pump’ [Roy, 2006]. The ‘manganese pump’ operates between an oxic and anoxic zone, where

Mn-oxides form in the oxic zone and dissolve in the anoxic zone. The anoxic zone becomes enriched in dissolved Mn^{2+}, and the dissolved Mn reacts with bicarbonates to form Mn-carbonates. Hence, evidence for Mo adsorption onto Mn-oxides will still be preserved in a redox stratified water column with oxic surface waters and anoxic bottom waters.

Another vector of Mo removal from the water column and transport to sediments is through adsorption onto Fe-oxides [Goldberg et al., 2009]. Similar to oxidized Mn-phases, the presence of Fe-oxides in BIFs also suggests the presence of oxygen; although Fe-oxides are a weaker proxy for molecular oxygen in the water column than Mn-oxides [Holland 2006; Buick, 2008]. Indeed, the presence of Fe-oxides serves as a weak indication for molecular oxygen because Fe-oxides are stable at a lower portion of the Eh-pH diagram than Mn-oxides, but more importantly, BIFs may have been produced by photoferrotrophic bacteria or ultraviolet photochemistry [Roy, 2006; Buick, 2008]. Photosynthetic oxidation notwithstanding, Fe-oxides will adsorb Mo in the water column; however, Mn-oxides more efficiently remove Mo and other metals from seawater because Mn-oxides are characterized by a low point of zero charge, and greater specific surface area and greater pore volume relative to Fe-oxides [Zhang et al., 2009; Matern and Mansfeldt, 2015]. Furthermore, Mn-oxides have a greater affinity for molybdate than phosphate, silicate, flouride, and sulfate, whereas Fe-oxides have a greater affinity for phosphate, and silicate than molybdate [Balistrieri and Chao, 1990]. Hence, in the presence of both Mn- and Fe-oxides in circum-neutral pH seawater and with a given ion chemistry, more molybdate will be adsorbed onto Mn-oxides, and this will be reflected in the sediments by a negative correlation between Fe/Mn and Mo concentrations. The

negative correlation observed between Fe/Mn and Mo concentrations in the Hotazel Formation thus suggests Mn-oxides were a more significant vector of Mo transport to sediments than Fe-oxides, but nonetheless, the relationship suggests Fe-oxides transported some Mo to sediments as well (Figure 3B).

While adsorption onto Fe- and Mn-oxides is a significant pathway for transferring Mo from seawater to sediment, Mo is not the only trace metal removed in this manner. In fact, an important mechanism for Co removal from the water column and transport to sediment is through adsorption onto Mn-oxide phases [Taillefert et al., 2002; Granados-Correa and Bulbulian, 2012]. Indeed, a close coupling between Co and Mn cycling has been observed in numerous modern lakes, where their concentrations throughout the water column are very strongly correlated, and a strong positive correlation between Co and Mn is observed in the Hotazel samples (Figure 3C) [Balistieri et al., 1992; Lienemann et al., 1997; Taillefert et al., 2002]. In addition, some studies indicate a positive coupling between Co and both Mn and Fe deposition; although experimental studies indicate Mn-oxides are likely a greater vector of Co transport to sediment than Fe-oxides [Murray and Dillard, 1979; Balistieri et al., 1986]. For example, particles enriched in Mn were shown to absorb more Co than Mn depleted particles, and Mn-oxides are characterized by a greater affinity for Co than Fe-oxides. During adsorption, Co(II) is oxidized to Co(III), and after oxidation to Co(III), it is hypothesized that Co is incorporated into the mineral structure [Crowther et al., 1983]. Indeed, additional spectroscopic studies verified this idea [Manceau et al., 1992a; Manceau et al., 1992b]. Furthermore, the strong coupling between these two elements may be because the oxidation of Co(II) occurs in the same Eh-pH space as Mn(II) oxidation, and as a result,

Mn(III,IV) oxides adsorb oxidized cobalt as they precipitate [Swanner et al., 2014]. Therefore, adsorption by Fe- and Mn-oxides may be a key vector of transport from the water column to sediments for both Co and Mo, and the strong negative correlation observed between Fe/Mn and Co concentrations provides further support for this argument (Figure 3D). Additionally, if the same removal mechanism is enriching sediments in both Mo and Co, there should be a correlation between their respective concentrations, and a strong correlation is observed between Co and Mo (Figure 4A).

In addition to Mo and Co, Ni also adsorbs onto Fe- and Mn-oxides [Boujelben et al., 2010; Green-Pedersen et al., 2010]. Moreover, the adsorption of Ni by Fe-and Mn-oxides is similar to the adsorption of Mo and Co in that Mn-oxides are more efficient in removing Ni from solution than Fe-oxides. Indeed, the maximum Ni adsorption capacities of Mn-oxides are ~20% greater than Fe oxides. Although the exact mechanism enabling Mn-oxides to adsorb more Ni than Fe-oxides is not known, it is likely a function of specific surface area, pore volume, and point of zero charge [Zhang et al., 2009; Matern and Mansfeldt, 2015]. Additionally, adsorption of Ni by Mn-oxides was determined to be more thermodynamically favorable than adsorption to Fe-oxides, where the Gibbs free energy value associated with adsorption to Mn-oxides is approximately 30% more negative than the value associated with adsorption to Fe-oxides [Boujelben et al., 2010]. The aforementioned geochemical attributes likely contribute to the strong negative correlation between Fe/Mn and Ni concentrations observed in the Hotazel Formation (Figure 4B). This relationship lends further support to the notion that Mn- and Fe-oxides were present in the water column and acted as a significant vector of trace metal transport to sediments.

Additionally, the adsorption of Sr to Mn- and Fe-oxide surfaces is well documented, and the correlation observed between Sr and Fe/Mn concentrations is likely the product of Sr adsorption onto the surfaces of these metal oxides (Figure 4C) [Axe et al., 2000; Pendelyuk et al., 2005; Park et al., 2012]. Indeed, adsorption enthalpies indicate Sr affinity to hydrous Mn-oxide surfaces is greater than that for hydrous Fe- or Al-oxide surfaces [Trivedi and Axe, 1999]. The competition for adsorption sites between Sr and non-radionuclides is not well studied; however, preliminary work indicates comparable adsorption capacities for both Sr and Co onto Mn-and Fe-oxide surface coatings [Park et al., 2012]. Furthermore, this work indicates the adsorption capacities for Sr and Co exceed that of Cs, but the adsorption capacities relative to other metals and ions are unknown. Therefore, in the absence of additional supporting data, the relationship observed between Sr and Fe/Mn concentrations in the Hotazel Formation is most readily explained by Sr adsorption onto the surfaces of Mn- and Fe-oxides.

While the abovementioned correlations suggest Mn- and Fe-oxide delivery of trace metals to sediments, it is very surprising that similar relationships are not present with other redox sensitive trace metals. After all, V readily absorbs onto Mn- and Fe-oxides, yet there are not even modest correlations between V and Mn, nor V and Fe [Tribovillard et al., 2006]. The lack of relationship is especially curious because vanadate oxyanions have been shown to be more competitive for sites on metal oxide surfaces than phosphate, arsenate, selenate, and molybdate [Huang et al., 2015]. Since the effects of other trace metals were ignored in the aforementioned study, it is possible that the presence of certain trace metals inhibits or precludes V adsorption. In addition, while there is a substantial body of work examining V adsorption onto metal oxides, there is a

paucity of studies examining the retention of V on metal oxide surfaces, and it is thus possible that the retention of V is very poor under certain conditions. Therefore, the mechanism(s) behind this apparent discrepancy may be resolved through future studies on the competitive adsorption and retention of V on Mn- and Fe-oxide surfaces.

Furthermore, Cr aquahydroxyl and hydroxyl cations readily adsorb to Mn- and Fe-oxides, but a relationship between Cr and Fe/Mn concentrations is absent from the data [Tribovillard et al., 2006]. Studies examining the oxidation of Cr in soils and aquatic environments have determined that the presence of additional trace metals and anions can interfere with Cr oxidation and adsorption [Richard and Bourg, 1991; Negra et al., 2005]. Indeed, anions commonly found in seawater such as HCO_3^-, Cl^-, SO_4^{2-}, HPO_4^{2-}, $H_2PO_4^-$, and MoO_4^{2-} can drastically reduce Cr(VI) adsorption [Richard and Bourg, 1991]. In addition, the oxidation of Cr in soils is inhibited by the presence of Mn, Co, Ni, Cu, and Pb, where Mn and Co were shown to have the strongest effect [Negra et al., 2005]. For example, the presence of Mn and Co can result in up to 70.5% and 58.9% less Cr oxidation, respectively. Hence, the lack of correlation between Cr and Fe/Mn may be the product of competitive ions in seawater depressing the adsorption of Cr by Mn- and Fe-oxides.

As a redox sensitive trace metal, U is often used as a paleoredox indicator, and it is somewhat surprising that only a weak correlation exists between Fe/Mn and U. Under oxic conditions, U is highly soluble and may be present in a host of U(VI) complexes [Sherman et al., 2008]. Moreover, U(VI) ions will adsorb onto Mn- and Fe-oxides [Sherman et al., 2008; Zou et al., 2011]. The primary U hosts in the crust include feldspars, zircon, apatite, and sphene, but notably, sulfides do not generally host U

[Anbar et al., 2007]. Although sulfide weathering is directly affected by oxygen content, oxygen content only has a mild impact on weathering of the primary U hosts. Therefore, dissolved U should have been present in the oceans at this point in time. The weak correlation between U and Fe/Mn correlations indicates that U may have been outcompeted for adsorption sites by other ions. Indeed, experimental work has shown that when the concentration of Zn(II) is increased from 0 to 40 ppm, the adsorption of U(VI) to manganese oxide surface coatings is reduced by 62%, and when the concentration of Cu(II) is increased from 0 to 40 ppm, the adsorption is reduced by 67% [Zou et al., 2011]. Furthermore, it has also been demonstrated that carbonate and bicarbonate ions will compete with U(VI) for adsorption sites on manganese oxide coatings [Han et al., 2007]. The effects of additional ions and trace metals on U(VI) adsorption have not been determined, but it is likely that competitive adsorption at Mn- and Fe-oxide surfaces was a contributing factor in the generation of the weak correlation between U and Fe/Mn concentrations.

Although the lack of correlation between Fe/Mn and V, Cr, and U is unexpected, perhaps the simplest and most probably explanation is that overall, Mn- and Fe-oxides have a greater affinity for Mo, Co, Ni, and Sr than V, Cr, and U. It is possible that only minimal empty surface sites remained for V, Cr, and U; hence a correspondingly minimal correlation is observed. Experimental work has shown that dissolved Mn^{2+} will also depress the adsorption and retention of other trace metals on manganese oxide surfaces, and since the water was at least periodically saturated with dissolved Mn^{2+}, this likely impacted the behavior of other trace metals. Comprehensive studies regarding the relative affinities of Mn- and Fe-oxides for the aforementioned trace metals are lacking in the

literature, and future studies of this nature may help elucidate the mechanisms driving the enrichments and correlations (or lack thereof) observed in the Hotazel Formation. In addition, since deposition of the Hotazel Formation was approximately coeval with the GOE, this indicates that oxidative weathering was not yet well established. Although the data suggest the Hotazel Formation was deposited within an oxygen oasis, atmospheric oxygen was still very low during this period of Earth's history. Since many trace metals are soluble in oxygenated waters and insoluble in oxygenated waters, the regional mineralogy may have impacted the trace metal enrichments of the depositional environment. For example, metals that were in low abundance or absent from the crust proximal to the depositional environment would have had to be transported by rivers to the ocean. On the oxygen deficient early Paleoproterozoic Earth, elements mobilized by oxidative weathering which become insoluble complexes under anoxic conditions were likely deposited very close to their sources. Therefore, the weak correlations between some metals and Fe/Mn may indicate that the sources of these metals were largely detrital, and they were only present as dissolved ions in very small proportions.

4.2 Mo Isotopes

In recent years, numerous studies have demonstrated Mo isotope fractionation induced by adsorption onto Mn- and Fe-oxide surfaces [Barling and Anbar, 2004; Wasylenki et al., 2008; Goldberg et al., 2009]. Results of laboratory work indicate that Mo adsorption by Mn- and Fe-oxides results in an equilibrium isotope effect, where lighter Mo isotopes are preferentially partitioned onto the adsorbent surface. Indeed, the

adsorption of molybdate by Mn-oxides is characterized by a fractionation of approximately -2.7 ‰, whereas the adsorption of molybdate by Fe-oxides is characterized by a smaller fractionation of approximately 0.83 to 2.19‰. In any case, the isotopic composition of Mo adsorbed onto the surfaces of Mn- and Fe-oxides will be lighter than that in solution. Furthermore, the δ^{98}Mo value of the modern ocean is 2.3‰, yet the isotopic composition of modern sediments range between approximately -0.7 and 2.3‰ [Barling et al., 2001; Siebert et al., 2003; Poulson et al., 2006; Siebert et al., 2006; Archer and Vance, 2008; Neubert et al., 2008]. Consistent with laboratory studies, the lightest isotopic signatures of the rock record are hosted within ferromanganese crusts and nodules. Conversely, the heaviest isotopic signatures are observed in euxinic sediments, and these values often overlap with the δ^{98}Mo value of the modern ocean. This overlap between the δ^{98}Mo value of euxinic sediments and seawater is produced by the near quantitative removal of molybdate from dominantly euxinic waters. Further, isotopic signatures intermediate of ferromanganese minerals and dominantly euxinic sediments are observed in suboxic sediments. The isotopic fractionations characterizing suboxic sediments are primarily driven by the transformation of molybdate to various thiomolybdate species [Tossel, 2005]. Indeed, quantum chemical computations indicate isotopic fractionations associated with the progressive sulfidation of molybdate to tetrathiomolybdate [Tossel, 2005]. Therefore, before interpreting isotope data with an eye towards tracking oxygen availability, it is necessary to discuss whether sulfur chemistry had an influence on the δ^{98}Mo values.

In the presence of H_2S, the following four step sulfidation process transforms molybdate into tetrathiomolybdate [Erickson and Helz, 2000]:

$MoO_4^{2-} \rightarrow MoO_3S^{2-} \rightarrow MoO_2S_2^{2-} \rightarrow MoOS_3^{2-} \rightarrow MoS_4^{2-}$

Each step of sulfidation is predicted to induce a fractionation of approximately -1.1‰ [Tossel, 2005]. Since thiomolybdate species are particle reactive and are removed from solution after adsorption onto humic substances and Mn-oxides or through uptake in authigenic Fe-sulfides, fractionation resulting from any degree of molybdate sulfidation may be preserved in marine sediments. To avoid misinterpreting the fractionation induced by progressive sulfidation as a signature produced by the adsorption of molybdate onto Mn- and Fe-oxides, it is essential to examine any evidence (or lack thereof) for the presence of H_2S in the depositional environment.

Bulk rock geochemical analyses of the Hotazel Formation have determined the major chemical constituents are SiO_2, Fe-oxides, CaO, and MgO, while MnO, Al_2O_3, Na_2O, and K_2O are present in negligible amounts less than 1 wt% [Tsikos and Moore, 1997; Tsikos et al., 2003]. Although XRD and XRF did not detect any sulfur species, microscope investigation determined minor pyrite components in the BIF layers but not the Mn ore; however, further work determined the pyrite is only hosted within carbonate-rich iron formations and ferromanganiferous carbonate units [Tsikos et al., 2003]. It is noteworthy that the samples for the present study were not derived from one of the carbonate-rich units, and therefore, there is no sign that they contain even a minor sulfur component. Hence, bulk rock geochemical and mineralogical analyses provide no indication that H_2S was present in the depositional environment.

In addition, the strong positive coupling between Mo and Co concentrations lends further support to the notion that the depositional environment was devoid of H_2S.

Indeed, a stark contrast exists between the geochemical behaviors of Mo and Co in the presence of H_2S [Algeo and Maynard, 2004; Swanner et al., 2014]. As stated previously, molybdate is converted to various sulfide complexes (thiomolybdates) in the presence of sulfide. Thiomolybdates are extremely particle reactive, and consequently, Mo enrichments in euxinic sediments can be up to 100 times greater than Mo concentrations of oxic sediments [Swanner et al., 2014]. In contrast, Co can form insoluble sulfides which may be taken up in solid solution with Fe-sulfides, but the kinetics of uptake are very slow [Bodin et al., 2007]. As a result, Co enrichments in euxinic sediments can be nearly an order of magnitude lower than Mo, and Co is thus described as having a weak euxinic affinity, whereas Mo is considered to have a strong euxinic affinity [Algeo and Maynard, 2004]. Indeed, field observations have further reinforced this classification by demonstrating that some Co will remain dissolved in sulfidic seawater, but Mo is quantitatively removed from solution if [H_2S] is in excess of 11μM [Neubert et al., 2008]. Hence, the contrasting geochemical attributes of Mo and Co under euxinic settings indicates the presence of H_2S should produce a decoupling in their deposition, yet a strong correlation is observed between their respective concentrations (Figure 4A). Furthermore, the negative correlation observed between Co and δ^{98}Mo indicates that adsorption onto Mn- and Fe-oxides offers a better explanation for the Mo isotope signatures than progressive sulfidation (Figure 5B). For example, if the isotopic signatures were induced by sulfidation of molybdate, then depleted δ^{98}Mo values should correlate with low Co concentrations, since Co has a weak euxinic affinity, and only weak Co enrichments are expected under sulfidic waters. Therefore, based on the above

arguments, there is no indication H_2S was present in the depositional environment, and it very unlikely that the δ^{98}Mo values were influenced by sulfidation.

The heaviest δ^{98}Mo value measured in the Hotazel Formation is 1.4 ‰, and this signature is hosted within the most Fe-rich sample. In contrast, the lightest δ^{98}Mo value measured in the Hotazel Formation is -1.15 ‰, and while this signature is hosted within a Mn-rich sample, it is not hosted within the most Mn-rich sample. Since $\Delta^{98}Mo_{soln\text{-}Ferrihydrite}$ equals ~1.1‰, $\Delta^{98}Mo_{soln\text{-}Magnetite}$ equals ~0.83‰, $\Delta^{98}Mo_{soln\text{-}Hematite}$ equals ~2.19 ‰, and $\Delta^{98}Mo_{soln\text{-}MnOx}$ is equal to ~2.7‰, a positive correlation is expected between Fe/Mn and δ^{98}Mo in a depositional environment where adsorption onto Fe- and Mn-oxides is a primary vector of Mo transport to sediments. Hence, the most straightforward interpretation of the relationship between Fe/Mn and δ^{98}Mo is that molybdate was removed from solution through adsorption onto Fe- and Mn-oxides. Furthermore, if the δ^{98}Mo value of seawater during deposition of the Hotazel was the same as the modern ocean, the δ^{98}Mo values of the samples are consistent with what is expected in an environment where Mo is primarily removed from the water column by adsorption to Fe- and Mn-oxides.

In order to compare the δ^{98}Mo values of the Hotazel with expected isotopic signatures based on experimentally determined fractionation factors and the δ^{98}Mo value of the modern ocean, the samples must first be categorized as either Fe-rich or Mn-rich. The Fe-rich samples are characterized by a greater proportion of Fe relative to Mn (Fe/Mn>1), and Mn-rich samples are characterized by a greater proportion of Mn relative to Fe (Fe/Mn<1). The average δ^{98}Mo value of the nine Fe-rich samples is 0.77 ‰, and the average δ^{98}Mo value of the fourteen Mn-rich samples is -0.16 ‰. These values

correspond well with the δ^{98}Mo values expected to ensue from the removal of molybdate by adsorption onto Fe- and Mn-oxides from seawater of approximately the same δ^{98}Mo value as the modern ocean.

While the average δ^{98}Mo signature of the Fe-rich samples falls on the isotopically light end of the spectrum of molybdenum isotope fractionation that is characteristic of molybdate adsorption onto Fe-oxides, this is readily explained by the Fe-mineralogy of the samples and/or a dilution of the isotopic signatures as a result of isotopically light Mo input by Mn-oxides. Indeed, the lightest δ^{98}Mo values produced by adsorption onto Fe-oxides are produced by adsorption onto hematite, and hematite is ubiquitously observed throughout the formation. Conversely, the fractionation factors associated with adsorption onto ferrihydrite, goethite, and magnetite are significantly less than for hematite, and neither ferrihydrite, goethite, nor magnetite are identified in the Hotazel; however, if hematite were the sole Fe-bearing mineral removing Mo from a seawater reservoir of approximately the same δ^{98}Mo signature as the modern ocean, a signature depleted by an additional ~0.5‰ would be expected [Tsikos et al., 1997; Tsikos et al., 2003]. Therefore, it is possible that ferrihydrite, goethite, and/or magnetite were initially present in the water column and sediments but underwent later phase transformations to hematite [Lagoeiro, 1998; Cudennec and Lecerf, 2006]. Furthermore, although these samples contain more Fe than Mn, they still contain a considerable fraction of Mn, and the isotopic signatures were likely diluted as Mn-oxides delivered Mo to sediments. Therefore, the isotopic signatures of the Fe-rich samples indicate that although hematite is the primary Fe-bearing mineral in the Hotazel Formation, magnetite, goethite, and/or ferrihydrite may also have been transporting adsorbed Mo to these sediments. Overall,

the simplest explanation for the average isotopic signature and the Fe mineralogy of the Hotazel is that multiple phases of Fe-bearing minerals transported Mo to sediments, and burial induced phase transformations produced the mineralogy present today.

Furthermore, the average δ^{98}Mo value of the Mn-rich samples is consistent with what is expected from the adsorption of molybdate onto Mn-oxide surfaces, assuming the δ^{98}Mo of the source molybdate had approximately the same isotopic composition as the molybdenum reservoir of the modern ocean. However, the isotopic signatures of the Mn-rich samples range from -1.15 to 0.41‰. A signature of 0.41‰ is only offset from the modern seawater value by ~1.9‰, and a signature of -1.15‰ is offset from the modern seawater value by ~3.4‰, so neither is in excellent agreement with $\Delta^{98}Mo_{soln\text{-}Mn\text{-}ox}$. In this case, it is instructive to compare the signatures measured in the Hotazel to signatures measured in modern environments. Indeed, the isotopic signatures of modern sediments in continental margins where dissolved oxygen is present do not exactly replicate the experimentally determined fractionation factor [Siebert et al., 2006; Poulson et al., 2006; Poulson et al., 2009]. Figure 6 illustrates a compilation of δ^{98}Mo values of modern sediments from various locations versus the oxygen content of their respective depositional environments. Not only does Figure 6 offer a semi-quantitative evaluation of the relationship between δ^{98}Mo and oxygen content, but it also illustrates that even in presence of oxygen, δ^{98}Mo values in natural settings will be offset from the fractionation factor. Further, a histogram of the isotope data from the Hotazel is displayed to the right of the plot in Figure 6, and the most frequently measured δ^{98}Mo values correspond to ~50-100 μM O_2.

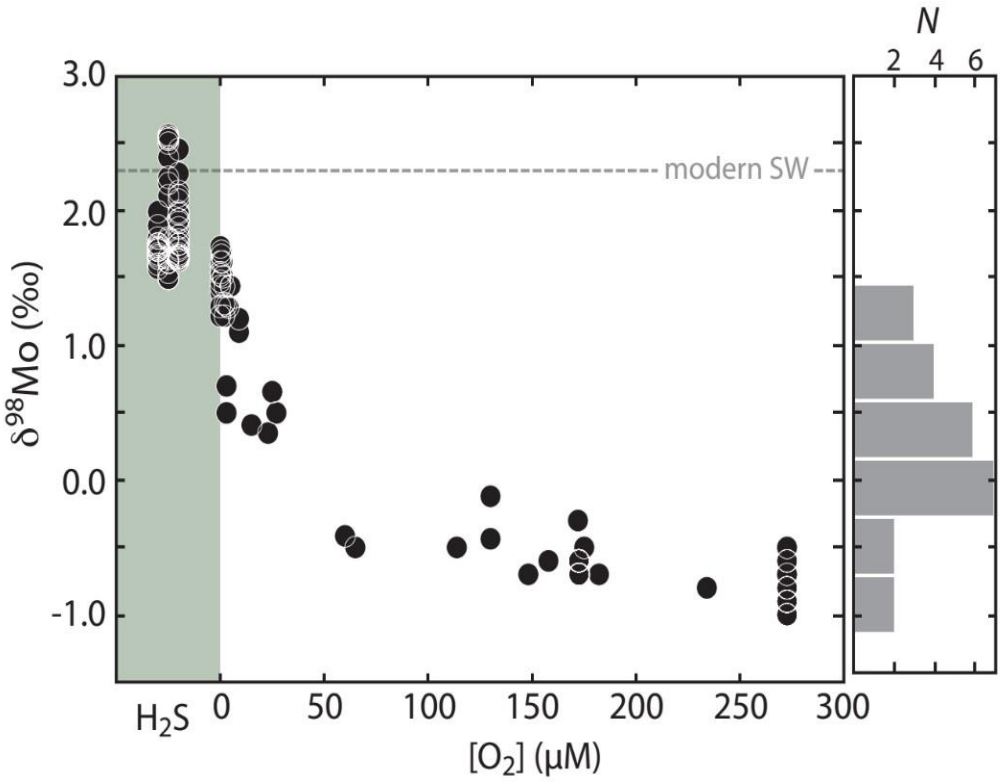

Figure 6. δ^{98}Mo values of modern sediments are plotted against the oxygen content [μM] of their respective depositional environments, and a histogram of the δ^{98}Mo values measured in the Hotazel Formation is plotted on the right. If the modern-day relationship between δ^{98}Mo and the oxygen content [μM] of the depositional environment was also prevalent during the deposition of the Hotazel, then seawater content may have periodically reached up to ~250 μM. [Data are taken from Siebert et al., 2006; Poulson et al., 2006; Neubert et al., 2008; Poulson et al., 2009].

The discrepancy between $\Delta^{98}Mo_{soln\text{-}Mn\text{-}ox}$ and δ^{98}Mo values measured in modern oxygenated sediments is in some cases suggested to be a function of dissolved sulfide in the pore waters, but as stated previously, there is no indication that dissolved sulfide was present in the depositional environment of the Hotazel. Therefore, it is unlikely that sulfide chemistry is influencing the isotopic signatures. While many oceanic locations are characterized by very low values of Mo input by means of terrestrial sedimentation, this

sedimentation can be large along the ocean-continent boundary [Poulson et al., 2009]. Further, the isotopic signatures characteristic of modern detrital materials range between -0.4 to 0.4 ‰, and it is possible that the relatively enriched isotopic signatures of the Mn-rich samples may have been influenced by detrital input [Siebert et al., 2006]. Indeed, multiple studies suggest the Hotazel, in addition to other formations in the Postmasburg Group and underlying Ghaap Group, were deposited in a marine shelf environment [Tsikos et al., 1997; Kirschvink et al., 2000; Johnson et al., 2013]. Thus, the contribution of detrital material may have been substantial enough to mildly dilute the δ^{98}Mo values produced by adsorption to Mn-oxides. To further support this argument, it is important to consider the state of the climate during deposition. As stated previously, the Hotazel was deposited during the aftermath of a snowball Earth event, and dropstones are observed in the basal units of the formation. If it is assumed that the isotopic signatures of the glacial sediments were similar to modern continental material, then it is plausible that this material may have diluted the isotopic signatures of the marine sediments.

At this point, it is important to consider that the δ^{98}Mo value of seawater may not have been the same as the modern value. In fact, it is possible that the divergence between $\Delta^{98}Mo_{soln\text{-}Mn\text{-}ox}$ and the measured δ^{98}Mo values of some of the samples was produced by distillation of the local Mo isotope reservoir. The Mo content of seawater during deposition was likely extremely low, since oxidative weathering was not fully established under the O_2-lean atmosphere, and oxidative weathering is the primary source of dissolved Mo to the oceans. Moreover, the deposition of the Hotazel Formation was a very unusual event, where eight billion metric tons of Mn ore were deposited in a single formation [Tsikos et al., 2003]. In an environment characterized by very high rates of

Mn- and Fe-oxide formation in addition to very low dissolved Mo concentrations, distillation may have temporarily driven the local δ^{98}Mo value of seawater to a larger value than today. In fact, a local seawater δ^{98}Mo value of ~3‰ would account for the Mn-rich samples containing the heaviest isotopic compositions. Furthermore, a greater δ^{98}Mo value of local seawater may offer an additional explanation for the offset between the average δ^{98}Mo of Fe-rich samples and $\Delta^{98}Mo_{soln\text{-}Hematite}$. Hence, the data suggest that the δ^{98}Mo value of local seawater may have temporarily become slightly more enriched than the modern signature.

While detrital input and distillation potentially influenced the δ^{98}Mo values of the Hotazel Formation, the offset between the experimentally determined fractionation factors and the measured isotopic compositions may have also been a product of geochemical cycling during diagenesis. Multiple studies have acknowledged the isotope effect that cycling within the sediment may induce, and secondary diagenetic processes will often produce increasingly fractionated isotopic signatures [Reitz et al., 2007; Poulson et al., 2009; Kurzweil et al., 2016]. Hence, the Mn-rich samples containing the most depleted isotopic compositions may have been produced by metal cycling in the sediments. As the oxygen content decreases in the sedimentary column, reductive dissolution of Mn- and Fe-oxides will ensue and thus release isotopically light Mo to pore waters and potentially the overlying water column. The re-liberated Mo, Mn^{2+}, and Fe^{2+} will diffuse to shallower sediment, and under oxidizing conditions, Mo will again adsorb onto Mn- and Fe-oxides [Siebert et al., 2006]. This cycling can produce further fractionations in the already depleted Mo in the pore waters, and therefore, this process may be responsible for the lightest signatures measured in the Mn-rich samples.

Further, multiple studies have suggested the Hotazel Formation was formed through alternating transgressive and regressive events that shifted the Mn^{2+}/Mn^{4+} redoxcline [Tsikos et al., 1997; Roy, 2000]. The Fe^{2+}/Fe^{3+} redoxcline is attained at lower Eh-pH than the Mn^{2+}/Mn^{4+} redoxcline, so Mn-oxides will dissolve before Fe-oxides as oxygen content decreases [Roy, 1988; Roy, 2000; Roy, 2006]. As a result of the differing redoxclines between Mn and Fe, a greater fraction of Mn-oxides may dissolve during diagenesis than Fe-oxides, and therefore, exchange of Mn and adsorbed Mo to the overlying water column may have produced a decoupling between Mn content and δ^{98}Mo values. The released Mn^{2+} can react with bicarbonate to form Mn-carbonates, but Mn-carbonates only constitute a minor component of the formation; hence, it is more plausible that re-liberated Mo and Mn^{2+} ions were adsorbed by Fe-oxides [Roy 2000; Han et al, 2012]. In any case, shifting sea level and redoxclines impacted the precipitation and dissolution of Mn- and Fe-oxides, so while it is difficult to predict exactly how this affected the isotope budget, it is probable that this dynamic environment contributed to some mild discrepancies in the data.

Altogether, the range of isotopic signatures preserved in the Mn-rich samples were potentially influenced by detrital input, distillation of the local δ^{98}Mo value of seawater, cycling during diagenesis, sea level fluctuations, or a combination of these mechanisms. It is acknowledged that there may be additional processes producing the widespread isotopic values of Mn-rich samples, but based on the available data, these are the preferred explanations. Therefore, taking into consideration the above discussions, the relationship observed between the δ^{98}Mo values and Fe/Mn concentrations (Figure 5A) is consistent with an oxygenated depositional environment in which Mn- and Fe-oxides

transported Mo to sediments. In addition, if we assume the relationship between δ^{98}Mo and oxygen content that is observed in modern depositional environments was also prevalent during the deposition of the Hotazel, then the oxygen content of local seawater may have been as high as ~250 μM (Figure 6). However, this estimate is based on the assumption that the δ^{98}Mo value of local seawater was approximately equivalent to the modern value, and as outlined above, the data are consistent with a δ^{98}Mo value of seawater that was comparable to the modern value or potentially heavier. If the seawater δ^{98}Mo value was heavier than that of the modern ocean, then the estimates of [O_2] here should be viewed as conservative.

Additionally, as outlined above, it has been demonstrated that Mn-oxides will efficiently scavenge Co and Ni from solution, and this study suggests the relationships between these elements and Fe/Mn concentrations may represent relatively unexplored paleoredox proxies. Since Mn-oxides remove light Mo isotopes, Co, and Ni from solution, negative relationships between δ^{98}Mo and both Co and Ni concentrations should develop in an environment where Mn-oxides deliver Mo, Co, and Ni to sediments (Figure 5B and 5C). Hence, the relationships between δ^{98}Mo, Co, and Ni provide further indications that Mn-oxides were present in the water column, and thus the water column was oxygenated.

4.3 Oxygenic Photosynthesis

Moreover, tracking the presence of Mn- and Fe-oxides using δ^{98}Mo values and Fe/Mn concentrations has been employed in previous work [Planavsky et al., 2014a;

Kurzweil et al., 2016]. These studies generally concluded that the positive correlation between δ^{98}Mo values and Fe/Mn concentrations provided evidence for the presence of O_2 in the water column 500 Ma before the GOE. Although the basis of this conclusion was strong and well supported, their approach for tracking molecular oxygen has never been applied to a post-GOE environment. Therefore, it has not previously been demonstrated that a positive relationship between δ^{98}Mo values and Fe/Mn concentrations is present in any depositional environment following the rise of atmospheric oxygen above 10^{-5} PAL. While experimental work and isotopic data from modern sediments have provided a robust framework supporting the application of δ^{98}Mo values and Fe/Mn concentrations for tracking molecular oxygen in ancient environments, a critical step in furthering bolstering the proxy and validating the findings of previous work is to establish the ability of the proxy to track the presence of molecular oxygen during a period of Earth's history during which it has already been unequivocally determined that O_2 was present in the atmosphere. Therefore, we compare the data from this study to the data from Planavsky et al., 2014a (Figure 5D). In fact, both datasets follow the same trend. Hence, the work here does not merely highlight the strength in using δ^{98}Mo values and Fe/Mn concentrations to track ancient oxygen availability, but it also buttresses the conclusions of Planavsky et al., 2014a. Indeed, data presented here are further support of oxygenic photosynthesis 500 Ma before the GOE.

Current estimates for the evolution of oxygenic photosynthesis are wide-ranging, but it is agreed that this metabolism must have evolved by ~2.4 Ga, since photosynthetic water-splitting is the only viable explanation for the extent of oxygen accumulation that culminated in the GOE [Knoll, 2015]. However, numerous studies

based on morphological features or geochemistry suggest the advent of oxygenic photosynthesis may have preceded the GOE by several hundred million years, and some studies even indicate an offset of nearly a billion years between the emergence of oxygenic photosynthesis and the GOE [Rosing et al., 1999; Schopf et al., 1993; Brocks et al., 1999; Allwood et al., 2006; Schopf and Kudryavtsev, 2012; Crowe et al., 2013]. Furthermore, phylogenetic analyses and molecular clock studies suggest the advent of oxygenic photosynthesis may have preceded the GOE by several hundred million years, but these estimates are very broad [Falcon et al., 2010; Schirrmeister et al., 2013]. Although there is substantial disagreement regarding the exact timing of this major metabolic innovation, numerous lines of evidence indicate that oxygenic photosynthesis must have preceded the GOE by at least several hundred million years. The results presented herein agree with the notion that the evolution of oxygenic photosynthesis predated the GOE, and more specifically, this evolutionary milestone was reached by at least 2.95 Ga.

It is important to note that the presence of Mn-oxides in the water column can also be explained without citing the presence of molecular oxygen. Before the evolution of water splitting photosynthesis, it is suggested that Mn^{2+} served as an electron donor for photosynthesis [Fischer et al., 2015]. In fact, the water oxidizing complex of photosystem II may have evolved from a transitional photosystem that oxidized Mn^{2+} [Johnson et al., 2013]. Although it is not possible to conclusively discount this hypothesis, several lines of evidence indicate the data are better explained by the presence of molecular oxygen produced by oxygenic photosynthesis. First, Mn deposits of this scale are not common in the geologic record, and Mn deposits of any scale are rare during the Archean [Roy,

2006]. If anoxygenic Mn-oxidizing phototrophy was capable of producing Mn deposits at the scale of the Hotazel formation, then it is curious that these deposits become more prevalent after this hypothesized transitional photosystem becomes extinct. Moreover, recent dating suggests the deposition of the Hotazel Formation was approximately coincident with the GOE [Gumsley et al., 2017]. The rise of atmospheric oxygen was not likely an immediate result of the evolution of oxygenic photosynthesis, but rather the product of oxygen sources overwhelming oxygen sinks [Lyons et al., 2014]. Hence, as stated previously, the evolution of oxygenic photosynthesis likely preceded the GOE by at least several hundred million years. Assuming that the phototrophic oxidation of Mn^{2+} served as a transitional stage in the evolution of oxygenic photosynthesis and produced large scale Mn deposits, the prevalence of Mn deposits should have been diminishing by the time of the deposition of the Hotazel Formation. Altogether, Mn oxidizing photosynthesis may very well have served as a transitional step to oxygenic photosynthesis, but it does not provide a satisfactory explanation for the deposition of the Hotazel Formation. Furthermore, photochemical Mn^{2+} oxidation is not an acceptable explanation for the presence of oxidized Mn phases in the water column during deposition because it has been shown that the photochemical oxidation of Mn^{2+} is precluded by the presence of dissolved Fe^{2+}, and the high concentration of Fe in the samples indicate an abundant supply of Fe^{2+} [Anbar and Holland, 1992]. Therefore, based on the aforementioned considerations and the data presented here, the preferred explanation for the deposition of the Hotazel Formation is by abiotic Mn- and Fe-oxide precipitation from an oxygenated water column.

CHAPTER 5: Summary and Conclusions

Data presented herein for the ~2.43-2.39 Ga Hotazel Formation are indicative of a locally oxygenated water column. Indeed, the evidence for a locally oxygenated water column is derived from a suite of paleoredox proxies involving trace metal enrichments and Mo isotope data. Since Mo, Co, Ni, and Sr are efficiently removed from solution and transported to sediment by Mn- and Fe-oxides, the strong correlations between their respective concentrations are interpreted as evidence for the presence of Mn- and Fe-oxides in the depositional environment. In addition, it is demonstrated that the Mo isotopic signatures were not influenced by sulfur chemistry, and the negative correlation between δ^{98}Mo values and Fe/Mn concentrations is utilized to further buttress the paleoredox indications provided by the concentration data alone. This study also employs relationships between δ^{98}Mo values and both Co and Ni concentrations as paleoredox indicators. Negative relationships between Mo isotope data and both Co and Ni concentrations provide additional support for the presence of Mn-oxides, but these data are also included to illustrate that Co and Ni represent promising yet relatively unexplored tools for tracking oxygen availability in ancient environments. Furthermore, based on the relationship between δ^{98}Mo values and oxygen content in modern sediments, it is estimated that local seawater may have reached up to ~250 μM [O_2] during deposition of the Hotazel Formation.

Furthermore, this is the first study attempting to track oxygen availability in a post-GOE environment through δ^{98}Mo values and Fe/Mn concentration data. Applying this method to sediments that were deposited after the rise of atmospheric oxygen is a critical step in validating the ability of this proxy to delineate the redox chemistry of ancient environments, and the results presented here affirm that the redox dependent relationship between δ^{98}Mo and Fe/Mn concentrations is capable of describing ancient oxygen availability. Moreover, the validation of this proxy is significant for previous work applying this oxygen tracking technique to 2.95 Ga iron stones. Indeed, the findings of the present study provide further support to the notion that oxygenic photosynthesis had evolved by at least 2.95 Ga. The work here may benefit from further application of paleoredox proxies to Hotazel samples. For example, Cr and V isotope analyses may provide further information regarding oxidative weathering and local ocean chemistry during the deposition of this formation. Furthermore, future work should use δ^{98}Mo and Fe/Mn concentrations, in addition to Co and Ni concentrations, to track ancient oxygen availability in additional paleoenvironments. Ultimately, as humans further explore our solar system and extrasolar worlds, application of the chemical signatures described herein represent a promising method for identifying the presence of ancient life forms.

References

Adelson, J.M.; Helz, G.R. and Miller, C.V., (2001), Reconstructing the rise of coastal anoxia; molybdenum in Chesapeake Bay sediments: *Geochimica et Cosmochimica Acta*, 65, 237-252.

Algeo, J.A. and Maynard J.M., (2004), Trace-element behavior and redox facies in core shales of Upper Pennsylvanian Kansas-type cyclothems: *Chemical Geology*, 206, 289-318.

Algeo, T.J. and Lyons, T.W., (2006), Mo-total organic carbon covariation in modern anoxic marine environments: Implications for analysis of paleoredox and paleohydrographic conditions: *Paleooceanography*, 21, PA1016., 1-21.

Allwood, A.C.; Walter, M.R.; Kamber, B.S.; Marshall, C.P. and Burch, I.W., (2006), Stromatolite reef from the Early Archaean era of Australia: *Nature*, 441, 714-718.

Anbar, A.D. and Holland, H.D., (1992), The photochemistry of manganese and the origin of banded iron formation: *Geochimica et Cosmochimica Acta*, 56, 2595-2603.

Anbar, A.D., (2004), Molybdenum stable isotopes: observations, interpretations, and directions: *Reviews in Mineralogy and Geochemistry*, 55, 429-454.

Anbar, A.D.; Duan, Y.; Lyons, T.W.; Arnold, G.L.; Kendall, B; Creaser, R.A.; Kaufman, A.J.; Gordon, G.W.; Scott, C.; Garvin, J. and Buick R., (2007), A whiff of oxygen before the Great Oxidation Event: *Science*, 317, 1903-1906.

Archer, C. and Vance, D., (2008), The isotopic signature of the global riverine molybdenum flux and anoxia in the ancient oceans: *Nature Geoscience*, 1, 597-600.

Arnold, G.L.; Anbar, A.D.; Barling, J. and Lyons, T.W., (2004), Molybdenum isotope evidence for widespread anoxia in Mid-Proterozoic oceans: *Science*, 304, 87-90.

Awramik, S.M. (1983), Filamentous fossil bacteria from the Archean of Western Australia: *Precambrian Research*, 20, 357-374.

Axe, L.; Tyson, T. and Morrison, T., (2000), Local structure analysis of strontium sorption to hydrous manganese oxides: *Journal of Colloid and Interface Science*, 224, 408-416.

Balistieri, L.S. and Murray, J.W., (1986), The surface-chemistry of sediments from the Panama Basin – the influence of Mn oxides on metal adsorption: *Geochimica et Cosmochimica Acta*, 50, 2235-2243.

Balistrieri, L.S. and Chao, T.T., (1990), Adsorption of selenium by amorphous iron oxyhydroxide and manganese dioxide: *Geochimica et Cosmochimica Acta*, 54, 739-751.

Balistrieri, L.S.; Murray, J.W.; and Paul, B., (1992), The biogeochemical cycling of trace metals in the water column of Lake Sammamish, Washington: Response to seasonally anoxic conditions: *Limnology and Oceanography*, 37(3), 529-548.

Barling, J.; Arnold, G.L. and Anbar, A.D., (2001), Natural mass-dependent variations in the isotopic composition of molybdenum: *Earth and Planetary Science Letters*, 193, 447-457.

Barling, J. and Anbar, A.D., (2004), Molybdenum isotope fractionation during adsorption by manganese oxides: *Earth and Planetary Science Letters*, 217, 315-329.

Bau, M.; Romer, R.L.; Luders, V.; and Beukes, N.J., (1999), Pb, O and C isotopes silicified Mooidraai dolomite (Transvaal Supergroup, South Africa): implications for the composition of Paleoproterozoic seawater and 'dating' the increase of oxygen in the Precambrian atmosphere: *Earth and Planetary Science Letters*, 174, 43-57.

Bau, M. and Alexander, B., (2006), Preservation of primary REE patterns without Ce anomaly during dolomitization of Mid-Paleoproterozoic limestone and the potential re-establishment of marine anoxia immediately after the "Great Oxidation Event": *South African Journal of Geology*, 109, 81-86.

Bertine, K.K. and Turekian, K.K., (1972), Molybdenum in marine deposits*: Geochimica et Cosmochimica Acta*, 37, 1415-1434.

Bodin, S.; Goden, A.; Matera, V.; Steinmann, P.; Vermeulen, J.; Gardin, S; Adatte, T.; Coccioni, R. and K.B. Föllmi, (2007), Enrichment of redox-sensitive trace metals (U, V, Mo, As) associated with late Hauterivian Faraoni oceanic anoxic event: *International Journal of Earth Sciences*, 96, 327-341.

Bond, D; Wignall, P.B. and Rack, G., (2004), Extent and duration of marine anoxia during the Frasnian-Famennian (Late Devonian) mass extinction in Poland, Germany, Austria and France: *Geological Magazine*, 141, 173-193.

Boujelben, N.; Bouzid, J.; Elouear, Z., and Feki, M., (2010), Retention of nickel from aqueous solutions using iron oxide and manganese oxide coated sand: kinetic and thermodynamic studies: *Environmental Technology*, 31, 1623-1634.

Brasier, M.D.; Green, O.R.; Jephcoat, A.P.; Kleppe, A.K.; Van Kranedonk, M.J.; Linsday, J.F.; Steele, A. and N.V. Grassineau, (2002), Questioning the evidence for Earth's oldest fossils: *Nature*, 416, 76-81.

Brasier, M.D.; Antcliffe, J.; Saunders, M. and D. Wacey, (2015), Changing the picture of Earth's earliest fossils (3.5-1.9 Ga) with new approaches and new discoveries: *Proceedings of the National Academy of Sciences of the United States of America*, 112, 4859-4864.

Brocks, J.J.; Logan, G.A.; Buick, R.; and Summons, R.E., (1999), Archean molecular fossils and the early rise of Eukaryotes: *Science*, 285, 1033-1036.

Buick, R., (2008), When did oxygenic photosynthesis evolve?: *Philosophical Transactions of the Royal Society B*, 363, 2731-2743.

Calvert, S.E. and Pedersen, T.F., (1993), Geochemistry of recent oxic and anoxic marine sediments: Implications for the geologic record*: Marine Geology*, 113, 67-88.

Canfield, D.E., (1998), A new model for Proterozoic ocean chemistry: *Nature*, 396, 450-453.

Canfield, D.E.; Poulton, S.W. and Narbonne, G.M., (2007), Late-Neoproterozoic deep-ocean oxygenation and the rise of animal life: *Science*, 315, 92-95.

Canfield, D.E.; Poulton, S.W.; Knoll, A.H.; Narbonne, G.M., Ross, G; Goldberg, T. and Strauss, H., (2008), Ferruginous conditions dominated later Neoproterozoic deep-water chemistry: *Science*, 321, 949-952.

Caruthers, A.H.; Smith, P.L. and Grocke D.R., (2013), The Pliensbachian-Toarcian (Early Jurassic) extinction, a global multi-phased event: *Palaeogeography, Palaeoclimatology, Palaeoecology*, 386, 104-118.

Catling, D.C.; Zahnle, K.J.; and McKay, C.P., (2001), Biogenic methane, hydrogen escape, and the irreversible oxidation of early Earth: *Science*, 293, 839-843.

Catling, D.C.; Glein, C.R., Zahnle, K.J.; and McKay, C.P., (2005), Why O_2 is required by complex life on habitable planets and the concept of planetary "oxygenation time": *Astrobiology*, 5(3), 415-438.

Chen, X.; Ling, H.; Vance, D.; Shields-Zhou, G.A.; Zhu, M.; Poulton, S.W.; Och, L.M.; Jiang, S.; Cremonese, L. and Archer, C., (2015), Rise to modern levels of ocean oxygenation coincided with Cambrian radiation of animals: *Nature Communications*, 6, 7142.

Clement, B.G.; Luther, G.W. and Tebo, B.M., (2009), Rapid, oxygen-dependent microbial Mn (II) oxidation kinetics at sub-micromolar oxygen concentrations in the Black Sea suboxic zone: *Geochimica et Cosmochimica Acta*, 73, 1878-1889.

Cornell, D.H., Schutte, S.S., Eglington, B.L., (1996), The Ongeluk basaltic andesite formation in Griqualand West, South Africa: submarine alteration in a 2222 Ma Proterozoic sea: *Precambrian Research*, 79, 101–123.

Crowe, S.A.; Dossing, L.N.; Beukes, N.J.; Bau, M.; Kruger, S.J.; Frei, R.; and Canfield, D.E., (2013), Atmospheric oxygenation three billion years ago: *Nature*, 501, 535-538.

Crowther, D.L.; Dillard, J.D., and Murray, J.W., (1983), The mechanism of Co(II) oxidation on synthetic birnessite: *Geochimica et Cosmochimica Acta*, 47, 1399-1403.

Cudennec, Y. and Lecerf, A., (2006), The transformation of ferrihydrite into goethite or hematite, revisited: *Journal of Solid State Chemistry*, 179, 716-722.

Czaja, A.D.; Johnson, C.M.; Roden, E.E.; Beard, B.L.; Voegelin, A.R.; Nagler, T.F.; Beukes, N.J. and Wille, M., (2012), Evidence for free oxygen in the Neoarchean ocean based on coupled iron-molybdenum isotope fractionation: *Geochimica et Cosmochimica Acta*, 86, 118-137.

Emerson, S.R. and Huested, S.S., (1991), Ocean anoxia and the concentrations of molybdenum and vanadium in seawater: *Marine Chemistry*, 34, 177-196.

Erickson, B.E. and Helz, G.R., (2000), Molybdenum (VI) speciation in sulfidic waters: stability and lability of thiomolybdates: *Geochimica et Cosmochimica Acta*, 64, 1149-1158.

Evans, D. A.; Beukes, N.J. and Kirschvink, J. L., (1997), Low-latitude glaciations in the Palaeoproterozoic era: *Nature (London)*, 386, 262–266.

Falcon, L.I.; Magallon, S., and Castillo, A., (2010), Dating the cyanobacterial ancestor of the chloroplast: *The International Society for Microbial Ecology*, 4, 777-783.

Farquhar, J., Bao, H. and Thiemens, M., (2000), Atmospheric influence of Earth's earliest sulfur cycle: *Science*, 289, 756-758.

Fischer, W.W.; Hemp, J., and Johnson, J.E., (2015), Manganese and the evolution of photosynthesis: *Origins of Life and Evolution of Biospheres*, 45, 351-357.

Goldberg, T.; Archer, C.; Vance, D. and Poulton, S.W., (2009), Mo isotope fractionation during adsorption to Fe (oxyhydr)oxides: *Geochimica et Cosmochimica Acta*, 73, 6502-6516.

Granados-Correa, F. and Bulbulian, S., (2012), Co(II) adsorption in aqueous media by a synthetic Fe-Mn binary oxide adsorbent: *Water Air Soil Pollution*, 223, 4089-4100.

Green-Pedersen, H.; Jensen, B.T. and Pind, N., (2010), Nickel adsorption on MnO2, (Fe(OH)3, montmorillonite, humic acid and calicite: A comparative study: *Environmental Technology*, 18, 807-815.

Gumsley, A.P.; Chamberlain, K.R.; Bleeker, W.; Soderlund, U.; de Kock, M.O.; Larsson, E.R. and Bekker, A., (2017), Timing and tempo of the Great Oxidation Event: *Proceedings of the National Academy of Sciences*, 114, 1811-1816.

Gutzmer, J., Beukes, N.J., (1996), Mineral paragenesis of the Kalahari manganese field: *South African Ore Geology Reviews*, 11, 405–428.

Han, R.; Zou, W.; Wang, Y. and Zhu, L., (2007), Removal of uranium(VI) from aqueous solutions by manganese oxide coated zeolite: discussion of adsorption isotherms and pH effect: *Journal of Environmental Radioactivity*, 93, 127-143.

Helz, G.R.; Miller, C.V.; Charnock, J.M.; Mosselmans, J.F.W.; Pattrick, R.A.D.; Garner, C.D. and Vaughan, D.J., (1996), Mechanism of molybdenum removal from the sea and its concentration in black shales: EXAFSevidence: *Geochimica et Cosmochimica Acta*, 60, 3631, 3642.

Holland, H.D., (2002), Volcanic gases, black smokers, and the Great Oxidation Event: *Geochimica et Cosmochimia Acta*, 66, 3811-3826.

Holland, H.D., (2006), The oxygenation of the atmosphere and oceans: *Philosophical Transactions of the Royal Society B-Biological Sciences*, 361, 903-915.

Hotinski, R.M.; Bice, K.L. and Kump L.R., (2001), Ocean stagnation and the end-Permian anoxia: *Geology*, 29, 7-10.

Huang, J.; Huang, F.; Evans, L. and Glasauer, S., (2015), Vanadium: global (bio)geochemistry: *Chemical Geology*, 417, 68-89.

Johnson, J.E.; Webb, S.M.; Thomas, K.; Ono, S.; Kirschvink, J.L. and Fischer, W.W., (2013), Manganese-oxidizing photosynthesis before the rise of cyanobacteria: *Proceedings of the National Academy of Sciences*, 110, 11238-11243.

Kashiwabara, T.; Takahashi, Y.; Tanimizu, M. and Usui, A., (2011), Molecular-scale mechanisms of distribution and isotopic fractionation of molybdenum between seawater and ferromanganese oxides: *Geochimica et Cosmochimica Acta*, 75, 5762-5784.

Kaufman, A.J.; Johnston, D.T.; Farquhar, J.; Masterson, A.L.; Lyons, T.W.; Bates, S.; Anbar, A.D.; Arnold, G.L.; Garvin, J. and Buick R., (2007), Late Archean biospheric oxygenation and atmospheric evolution: *Science*, 317, 1900-1903.

Kendall, B.; Reinhard, C.T.; Lyons, T.W.; Kaufman, A.J.; Poulton, S.W. and Anbar, A.D., (2010) Pervasive oxygenation along late Archaean ocean margins: *Nature Geoscience*, 3, 647-651.

Kendall, B; Komiya, T; Lyons, T.W.; Bates, S.M.; Gordon, G.W.; Romaniello, S.J.; Jiang, G.; Creaser, R.A.; Xiao, S.; Mcfadden, K.; Sawaki, Y.; Tahata, M.; Shu, D.; Han, J.; Li, Y.; Chu, X. and Anbar, A.D., (2015), Molybdenum isotope evidence for an episode of widespread ocean oxygenation during the late Ediacaran Period: *Geochimica et Cosmochimica Acta*, 156, 173-193.

Kirschvink, J.L.; Gaidos, E.J.; Bertani, L.E.Beukes, N.J.; Gutzmer, J.; Maepa, L.N. and Steinberger, R.E., (2000), Paleoproterozoic snowball Earth: extreme climatic and geochemical global change and its biological consequences: *Proceedings of the National Academy of Sciences*, 97, 1400-1405.

Knoll, A.H.; Bambach, R.K.; Canfield, D.E. and Grotzinger, J.P., (1996), Comparative Earth history and late Permian mass extinction: *Science*, 273, 452-457.

Knoll, A.H., (2014), Paleobiological perspectives on early eukaryotic evolution: *Cold Spring Harbor Perspectives in Biology*, 6(1):a016121.

Knoll, A.H., (2015), Paleobiological perspectives on early microbial evolution: *Cold Spring Harbor Perspectives in Biology*, 7:a018093

Kopp, R.E.; Kirschvink, J.L.; Hillburn, I.A. and Nash, C.Z., (2005), The paleoproterozoic snowball Earth: a climate disaster triggered by the evolution of oxygenic photosynthesis: *Proceedings of the National Academy of Sciences*, 102, 11131-11136.

Kump, L.R. and Barley, M.E., (2007), Increased subaerial volcanism and the rise of atmospheric oxygen 2.5 billion years ago: *Nature*, 448, 1033-1035.

Kurzweil, F.; Wille, M.; Gantert, N.; Beukes, N.J. and Schoenberg, R., (2016), Manganese oxide shuttling in pre-GOE ocean – evidence from molybdenum and iron isotopes: *Earth and Planetary Science Letters*, 452, 69-78.

Lagoeiro, L.E., (1998), Transformation of magnetite to hematite and its influence on the dissolution of iron oxide minerals: *Journal of Metamorphic Geology*, 16, 415-423.

Lane, N. and Martin, W., (2010), The energetics of genome complexity: *Nature*, 467, (929-934.

Lienemann, C.P.; Taillefert, M.; Perret, D. and Gaillard, J, (1997), Association of cobalt and manganese in aquatic systems: chemical and microscopic evidence: *Geochimica et Cosmochimica Acta*, 61, 1437-1446.

Lyons, T.W.; Planavsky, N.J. and Reinhard, C.T., (2014), The rise of oxygen in Earth's early ocean and atmosphere: *Nature*, 506, 307-315.

McManus, J.; Berelson, W.M.; Severmann, S.; Poulson, R.L.; Hammond, D.E.; Klinkhammer, G.P. and Holm, C., (2006), Molybdenum and uranium geochemistry in continental margin sediments: paleoproxy potential: *Geochimica et Cosmochimica Acta*, 70, 4643-4662.

Manceau, A.; Gorshkov, A.I. and Brits, V.A., (1992a), Structural chemistry of Mn, Fe, Co, and Ni in manganese hydrous oxides: Part I., Information from XANES spectroscopy: *American Mineralogy*, 77, 1144-1157.

Manceau, A.; Gorshkov, A.I. and Brits, V.A., (1992b), Structural chemistry of Mn, Fe, Co, and Ni in manganese hydrous oxides: Part II. Information from EXAFS spectroscopy and electron and X-ray diffraction: *American Mineralogy*, 77, 1144-1157.

Matern, K. and Mansfeldt, T., (2015), Molybdate adsorption by birnessite: *Applied Clay Science*, 108, 78-83.

Moore, J.M.; Tsikos, H. and Polteau, S., (2001), Deconstructing the Transvaal Supergroup, South Africa: implications for Palaeoproterozoic palaeoclimate models: *Journal of African Earth Sciences*, 33, 437-444.

Morford, J.L. and Emerson, S., (1999), The geochemistry of redox sensitive trace metals in sediments: *Geochimica et Cosmochimica Acta*, 63, 1735-1750.

Morse, J.W. and Luther, G.W., (1999), Chemical influences on trace metal-sulfide interactions in anoxic sediments: *Geochimica et Cosmochimica Acta*, 63, 3373-3378.

Murray, J.W. and Dillard, J.G., (1979), Oxidation of cobalt (II) adsorbed on manganese-dioxide: *Geochimica et Cosmochimica Acta*, 43, 1979.

Neubert, N.: Nagler, T.F. and Bottcher, M.E., (2008), Sulfidity controls molybdenum isotope fractionation into euxinic sediments: evidence from the modern Black Sea: *Geology*, 36, 775-778.

Negra, R.; Ross, D.S. and Lanzirotti, A., (2005), Oxidizing behavior of soil manganese: interactions among abundance, oxidation state, and pH: *Soil Science Society of America*, 69, 87-95.

Nursall, J.R., (1959), Oxygen as a prerequisite to the origin of the Metazoa: *Nature*, 183, 1170-1172.

Olson, S.L.; Kump, L.R. and Kasting, J.F., (2013), Quantifying the areal extent and dissolved oxygen concentrations of Archean oxygen oases: *Chemical Geology*, 362, 35-43.

Park, Y.; Shin, W. and Choi, S., (2012), Sorptive removal of cobalt, strontium and cesium onto manganese and iron oxide coated montmorillonite from groundwater: *Journal of Radioanalytical Nuclear Chemistry*, 292, 837-852.

Pendelyuk, O.I.; Lisnycha, T.V.; Strelko, V.V. and Kirillov, S.A., (2005), Amorphous MnO_2-TiO_2 composites as sorbents for Sr^{2+} and UO_2^{2+}: *Adsorption-Journal of the International Adsorption Society*, 11, 799-804.

Planavsky, N.J.; Asael, D.; Hofmann, A., Reinhard, C.T.; Lalonde, S.V.; Knudsen, A.; Wang, X.; Ossa Ossa, F.; Pecoits, E.; Smith, A.J.B.; Beukes, N.J.; Bekker, A.; Johnson, T.M.; Konhauser, K.O.; Lyons, T.W. and Rouxel, O.J., (2014a), Evidence for oxygenic photosynthesis half a billion years before the Great Oxidation Event: *Nature Geoscience*, 7, 283-286.

Planavsky, N.J.; Reinhard, C.T.; Wang, X.; Thomson, D.; McGoldrick, P.; Rainbird, R.H.; Johnson, T.; Fischer, W.W. and Lyons, T.W., (2014b), Low Mid-Proterozoic atmospheric oxygen levels and the delayed rise of animals: *Science*, 346, 635-638.

Poulson, R.L.; Siebert, C.; McManus, J. and Berelson, W.M., (2006), Authigenic molybdenum isotope signatures in marine sediments: *Geology*, 34, 617-620.

Poulson, R.L.; McManus, J.; Severmann, S. and Berelson W.M., (2009), Molybdenum behavior during early diagenesis: insights form Mo isotopes: *Geochemistry, Geophsics, Geosystems*, 10, 1-25.

Rashby, S.E.; Sessions, A.L.; Summons, R.E. and Newman, D.K., (2007), Biosynthesis of 2-methylbacteriohopanepolyols by an anoxygenic phototroph: *Proceedings of the National Academy of Sciences*, 104, 99-104.

Rasmussen, B.; Fletcher, I.R.; Brocks, J.J. and M.R. Kilburn, (2008), Reassessing the first appearance of eukaryotes and cyanobacteria: *Nature*, 455, 1101-1104.

Reinhard, C.T.; Planavsky, N.J.; Olson, S.L.; Lyons, T.W. and D.H. Erwin, (2016), Earth's oxygen cycle and the evolution of animal life: *Proceedings of the National Academy of Sciences*, 113, 8933-8938.

Reitz, A.; Wille, M.; Nagler, T.F. and de Lange G.J., (2007), Atypical Mo isotope signatures in eastern Mediterranean sediments: *Chemical Geology*, 245, 1-8.

Richard, F.C. and Bourg, A.C.M., (1991), Aqueous geochemistry of chromium: a review: *Water Research*, 25, 807-816.

Rosing, M.T., (1999), 13C-depleted carbon microparticles in >3700-Ma sea-floor sedimentary rocks from West-Greenland: *Science*, 283, 674-676.

Roy, S., (1988), Manganese metallogenesis: a review: *Ore Geology Reviews*, 4, 155-170.

Roy, S., (2000), Late Archean initiation of manganese metallogenesis: its significance and environmental controls: *Ore Geology Reviews*, 17, 179-198.

Roy, S., (2006), Sedimentary manganese metallogenesis in response to the evolution of the Earth system: *Earth Science Reviews*, 77, 273-305.

Scott, C; Lyons, T.W.; Bekker, A.; Shen, Y.; Poulton, S.W.; Chu, X. and Anbar, A.D., (2008), Tracing the stepwise oxygenation of the Proterozoic ocean: *Nature*, 452, 456-459.

Scott, C., and Lyons, T.W., (2012), Contrasting molybdenum cycling and isotopic properties in euxinic versus non-euxinic sediments and sedimentary rocks: refining the paleoproxies: *Chemical Geology*, 324-325, 19-27.

Schirrmeister, B.E.; de Vos, J.M.; Antonelli, A. and Bagheri, H.C., (2013), Evolution of multicellularity coincided with increased diversification of cyanobacteria and the Great Oxidation Event: *Proceedings of the National Academy of Sciences*, 110, 1791-1796.

Schopf, J.W. and Packer, M.B., (1987), Early Archean (3.3-Billion to 3.5-Billion-Year-Old) microfossils from Warrawoona Group, Australia: *Science*, 237, 70-73.

Schopf, J.W., (1993), Microfossils of the early Archean Apex Chert: new evidence of the antiquity of life: *Science*, 260, 640-646.

Schopf, J.W.; Kudryavtsev, A.B.; Agresti, D.G.; Wkowiak, T.J. and Czaja, A.D., (2002), Laser-Raman imagery of Earth's earliest fossils: *Nature*, 416, 73-76.

Schopf, J.W. and Kudryavtsev, A.B., (2012), Biogenicity of Earth's earliest fossils: A resolution of the controversy: *Gondwana Research*, 22, 761-771.

Sherman, D.M.; Peacock, C.L. and Hubbard C.G., (2008), Surface complexation of U(VI) on goethite (α-FeOOH): *Geochimica et Cosmochimica Acta*, 72, 298-310.

Siebert, C.; Nagler, T.F.; Von Blanckenburg, F. and Kramers, J.D., (2003), Molybdenum isotope records as a potential new proxy for paleooceanography: *Geochimica et Cosmochimica Acta*, 211, 159-171.

Siebert, C.; McManus, J.; Bice, A.; Poulson, R. and Berelson, W.M., (2006), Molybdenum isotope signatures in continental margin marine sediments: *Earth and Planetary Science Letters*, 241, 723-733.

Summons R.E.; Jahnke, L.L.; Hope, J.M. and Logan G.A. (1999), 2-Methylhopanoids as biomarkers for cyanobacterial oxygenic photosynthesis: *Nature*, 400, 554-557.

Swanner, E.D.; Planavsky, N.J.; Lalonde, S.V.; Robbins, L.J.; Bekker, A.; Rouxel, O.J.; Saito, M.A.; Kappler, A.; Mojzsis, S.J. and Konhauser K.O., (2014), Cobalt and marine redox evolution: *Earth and Planetary Science Letters*, 390, 253-263.

Taillefert, M.; Macgregor, B.J.; Gaillard, J.F.; Lienemann, C.P.; Perret, D. and Stahl, D.A., (2002), Evidence for a dynamic cycle between Mn and Co in the water column of a stratified lake: *Environmental Science and Technology*, 36, 468-476.

Tossel, J.A., (2005), Calculating the partitioning of isotopes of Mo between oxidic and sulfidic species in aqueous solution: *Geochimica et Cosmochimica Acta*, 69, 2981-2993.

Tribovillard, N.; Algeo, T.J.; Lyons, T.W. and Ribouleau, A., (2006), Trace metals as paleoredox and paleoproductivity proxies: an update: *Chemical Geology*, 232, 12-32.

Trivedi, P. and Axe, L., (1999), A comparison of strontium sorption to hydrous aluminum, iron, and manganese oxides: *Journal of Colloid and Interface Science*, 218, 554-563.

Tsikos, H. and Moore, J.M., (1997), Petrography and geochemistry of the Paleoproterozoic Hotazel Iron-Formation, Kalahari, manganese field, South Africa: implications for Precambrian manganese metallogenesis: *Economic Geology*, 92, 87-97.

Tsikos, H., Beukes, N.J., Moore, J.M., Harris, C., (2003), Deposition, diagenesis, and secondary enrichment of metals in the Palaeoproterozoic Hotazel Iron Formation, Kalahari manganese field: *South African Journal of Economic Geology*, 98, 1449–1462.

Tsikos, H.; Matthews, A.; Erel, Y. and Moore, J.M., (2010), Iron isotopes constrain biogeochemical redox cycling of iron and manganese in a Palaeoproterozoic stratified basin: *Earth and Planetary Science Letters*, 298, 125-134.

Wasylenki, L.E.; Rolfe, B.A.; Weeks, C.L.; Spiro, T.G. and Anbar A.D., (2008), Experimental investigation of the effects of temperature and ionic strength on Mo isotope fractionation during adsorption to manganese oxides: *Geochimica et Cosmochimica Acta*, 72, 5997-6005.

Wignall, P.B. and Hallman, A., (1992), Anoxia as a cause of the Permian-Triassic mass extinction: facies evidence from northern Italy and the western United States: *Palaeogeography, Palaeoclimatology, Palaeoecology*, 93, 21-46.

Wignall, P.B. and Twitchett, R.J., (1996), Oceanic anoxia and the end Permian mass extinction: *Science*, 272, 1155-1158.

Van de Schootbrugge, B; McArthur, J.M.; Bailey, T.R.; Rosenthal, Y.; Wright, J.D. and Miller, K.G., (2005), Toarcian oceanic anoxic event: an assessment of global causes using belemnite C isotope records: *Paleoceanography*, 20, PA3008.

Zhang, G.; Liu, H.; Lliu, R. and Qu, J., (2009), Adsorption behavior and mechanism of arsenate at Fe-Mn binary oxide/water interface: *Journal of Hazardous Materials*, 168, 820-825.

Zou, W.; Zhao, L. and Han, R., (2011), Adsorption characteristics of uranyl ions by manganese oxide coated sand in batch mode: *Journal of Radioanalytical Nuclear Chemistry*, 288, 239-249.